Crustal velocity structure of the Lucky Strike segment of the Mid-Atlantic Ridge at 37°N from seismic refraction measurements

T. Seher, W. C. Crawford, S. C. Singh, M. Cannat, V. Combier, D. Dusunur

JOURNAL OF GEOPHYSICAL RESEARCH, VOL. 115, B03103, doi:10.1029/2009JB006650, 2010

Crustal velocity structure of the Lucky Strike segment of the Mid-Atlantic Ridge at 37°N from seismic refraction measurements

Tim Seher,[1,2] Wayne C. Crawford,[1] Satish C. Singh,[1] Mathilde Cannat,[1] Violaine Combier,[1] and Doga Dusunur[1]

Received 27 May 2009; revised 26 October 2009; accepted 28 September 2009; published 19 March 2010.

[1] We estimate the seismic structure of the slow spreading Lucky Strike segment of the Mid-Atlantic Ridge, located approximately 300 km south of the Azores platform, using seismic reflection and seismic refraction data acquired in June 2005 as a part of the Seismic Study for Monitoring of the Mid-Atlantic Ridge (SISMOMAR) survey. The three-dimensional velocity model shows an upper crustal low-velocity anomaly running parallel to the ridge axis, which is limited by the median valley bounding faults. The velocity models also show a low-velocity anomaly underlying the axial melt lens reflector located at the segment center below the Lucky Strike volcano. This lower crustal low-velocity region can be explained by elevated temperatures and possibly small amounts of melt. The lower crustal low-velocity anomaly and the axial melt lens reflector constrain the geometry of the magma chamber responsible for the construction of the Lucky Strike volcano. The presence of this magma chamber and thick crust at the segment center are consistent with a focused melt supply to the segment center.

Citation: Seher, T., W. C. Crawford, S. C. Singh, M. Cannat, V. Combier, and D. Dusunur (2010), Crustal velocity structure of the Lucky Strike segment of the Mid-Atlantic Ridge at 37°N from seismic refraction measurements, *J. Geophys. Res.*, *115*, B03103, doi:10.1029/2009JB006650.

1. Introduction

[2] The morphology, and presumably the magma supply, of mid-ocean ridges varies dramatically with spreading rate. Ridges with slow spreading rates typically have a deep rift valley, whereas axial highs are commonly observed at fast spreading rates [*Macdonald*, 2001]. This difference is usually explained as the result of a greater magma supply at fast spreading ridges, a hypothesis that is further supported by the presence of axial highs at sections of slow spreading ridges that are close to hot spots [*Keeton et al.*, 1997; *Sinha et al.*, 1998]. Modeling studies preclude the existence of large, steady state magma bodies beneath slow spreading ridge [*Sleep*, 1975; *Kusznir and Bott*, 1976]. Presumably, crustal accretion at fast spreading ridges is dominated by magmatic processes whereas accretion at slow spreading ridges has a much larger tectonic component [*Cannat et al.*, 1995].

[3] Detailed studies of fast spreading ridges such as the East Pacific Rise and the Galápagos Ridge reveal widespread high-temperature hydrothermal circulation and crustal magma chambers [e.g., *Weiss et al.*, 1977; *Corliss et al.*, 1979; *Spiess et al.*, 1980; *Detrick et al.*, 1987; *Harding et al.*, 1993; *Dunn and Toomey*, 1997; *Blacic et al.*, 2004]. While hydrothermal venting has been observed along slow spreading ridges like the Mid-Atlantic Ridge (MAR) [e.g., *Karson and Brown*, 1988; *Lalou et al.*, 1990], axial magma bodies have so far only been imaged at the hot spot influenced Reykjanes Ridge (57°50′N) [*Navin et al.*, 1998; *Sinha et al.*, 1998], possibly the Snakepit Ridge [e.g., *Detrick et al.*, 1990; *Calvert*, 1995, 1997; *Canales et al.*, 2000] and, recently, the Lucky Strike segment [*Singh et al.*, 2006].

[4] One of the problems with comparing fast and slow spreading plate boundaries is that there have been far fewer seismic studies quantifying the crustal structure of slow spreading plate boundaries such as the MAR, in part not only because more ''interesting'' structure (i.e., magma chambers) has been found at fast spreading ridges, but also because slow spreading ridges have a more complicated structure, which makes them both more difficult to image seismically and more difficult to generalize any results obtained. To date, only two MAR segments have been seismically imaged in three dimensions down to the crust-mantle boundary or Mohorovièić discontinuity (Moho): the Reykjanes Ridge at 57°50′N [*Navin et al.*, 1998; *Sinha et al.*, 1998] and the OH-1 segment at 35°N [*Magde et al.*, 1997; *Barclay et al.*, 1998; *Dunn et al.*, 2005]. Interestingly, both of these segments show evidence of crustal melt, indicating that magmatism can play a role in crustal accretion at slow spreading ridges.

[5] We report on the three-dimensional (3-D) seismic structure of the Lucky Strike segment of the MAR (37°N) using data acquired during the 2005 Seismic Study for

[1]Institut de Physique du Globe de Paris, Géosciences Marines, Paris, France.
[2]Now at Earth Resources Laboratory, Massachusetts Institute of Technology, Cambridge, Massachusetts, USA.

0148-0227/10/2009JB006650

Monitoring of the Mid-Atlantic Ridge (SISMOMAR) experiment. The combination of a high-temperature hydrothermal venting site on top of the segment's central volcano and a well-defined axial valley with numerous surface faults [*Langmuir et al.*, 1997; *Humphris et al.*, 2002; *Escartín et al.*, 2008; *Ondréas et al.*, 2009] makes this segment a prime candidate for studying the role of magmatism, hydrothermal circulation, and tectonics in crustal accretion at a slow spreading mid-ocean ridge. We used an array of ocean bottom seismometers (OBS) and a grid of air gun shots covering the median valley and bounding walls, with sensitivity out to the segment ends. We analyzed crustal turning rays (Pg) and crust-mantle boundary reflections (PmP) to obtain a 3-D model of the crustal velocity structure and the depth to the crust-mantle boundary. The model reveals a low-velocity region in the lower crust underneath the axial melt lens reflector, along-axis crustal thinning, and a significant upper crustal velocity increase away from the axial valley.

2. Lucky Strike Segment

[6] The Lucky Strike segment (Figure 1) is located at 37°N on the MAR, just south of the Azores hot spot and between the Menez Gwen and Famous segments. It is approximately 70 km long and is delimited by nontransform offsets [*Parson et al.*, 2000]. It has a 15–20 km wide median valley and a large volcano at the segment center. This volcano indicates a relatively robust magma source, whereas the median valley and segment parallel faults indicate that tectonism plays an important role in crustal accretion. For comparison, the Menez Gwen segment, just to the north, has no rift valley, and the magmatism is focused at shallow volcanoes at the segment center [*Ondréas et al.*, 1997], whereas the North Famous segment, just to the south, has a deep median valley and no central seamount. On the basis of the axial valley relief and mantle Bouguer gravity anomalies, *Thibaud et al.* [1998] suggest that the Lucky Strike is in an intermediate thermal state between the relatively hot Menez Gwen and relatively cold North Famous segments. Furthermore, the Menez Hom Massif [*Fouquet et al.*, 2002; *Marques et al.*, 2007] at the southern end of the Lucky Strike segment shows exhumed ultramafic rocks at the seafloor, which indicates a relatively cold thermal regime.

[7] The Lucky Strike segment is currently either in a magmatically active phase or in transition from a magmatic to a more tectonic phase. There is significant evidence for recent magmatism: the main volcano holds a fresh lava lake [*Fouquet et al.*, 1995; *Humphris et al.*, 2002], which unlike terrestrial lava lakes has been very short lived [*Ondréas et al.*, 2009]. A volcanic edifice extending northwest from the volcano, the western volcanic ridge, has recent pillow lavas [*Fouquet et al.*, 1994]. An earthquake swarm recorded on the segment by a regional hydrophone array in 2001 is likely to be linked to a dike injection [*Dziak et al.*, 2004]. If diking events there are similar to those recently documented on the slow spreading plate boundaries in Iceland [*Buck et al.*, 2006] and Ethiopia [*Wright et al.*, 2006; *Doubre et al.*, 2007], both of which propagated for tens of kilometers, the dikes could propagate from the segment center to the segment end. A mantle Bouguer anomaly bull's-eye at the segment center suggests focused melt delivery and thickened crust [*Detrick et al.*, 1995; *Thibaud et al.*, 1998; *Cannat et al.*, 1999; *Escartín et al.*, 2001].

[8] The observed volcanism might also be influenced by the proximity of the Azores hot spot [*Langmuir et al.*, 1997]. *Cannat et al.* [1999] and *Escartín et al.* [2001] observe V-shaped ridges propagating south from the Azores hot spot and two anomalously shallow regions, the eastern and western Jussieu plateau, which are located on either side of the MAR at the same latitudes as the Famous and Lucky Strike segments. These bathymetric and gravimetric anomalies are usually linked to augmented melt supply from a hot spot [*Cochran and Talwani*, 1978; *Le Douaran and Francheteau*, 1981; *Cannat et al.*, 1999; *Escartín et al.*, 2001; *Ito*, 2001], which explains the formation of the Jussieu plateau 10–4 Ma ago during a period of enhanced magmatism due to the southward propagation of a melting anomaly originating at the Azores hot spot [*Cannat et al.*, 1999]. Furthermore, *Moreira and Allègre* [2002] show an influence of hot spot derived melt on the MAR south of the Azores based on rare-gas analyses. On the basis of teleseismic observations *Yang et al.* [2006] propose that the melt from the Azores mantle plume is deflected toward the southern MAR by asthenospheric flow and plate motion.

[9] There is evidence, however, that the Lucky Strike segment does not have significantly enhanced melt supply as compared to other MAR segments farther to the south. Raised bathymetry around the Azores hot spot is observed to at least 26°30′N [*Thibaud et al.*, 1998], about 1600 km south of the hot spot, and far south of the Lucky Strike segment. In addition, the spreading axis is much deeper than the surrounding plateau and splits the Jussieu plateau in two. Also, the segment's along-axis mantle Bouguer anomaly and bathymetric variation are relatively weak, which has been interpreted to suggest that it has a lower magma supply than do several segments that lie much farther from the Azores Plateau [*Thibaud et al.*, 1998].

[10] A field of high-temperature hydrothermal vents sits at the summit of Lucky Strike volcano [*Langmuir et al.*, 1997]. Using observations of sulfide rubble, *Humphris et al.* [2002] argue that the hydrothermal systems have been active for hundreds to thousands of years. A 3-D resistivity model derived from controlled source electromagnetics shows low resistivity anomalies underneath and to the north of the Lucky Strike volcano [*Barker*, 2004]. These decreased resistivities are likely related to an increase in porosity and permeability, which might play an important role in the hydrothermal fluid flow. The vents provide a significant contribution to the near-axis heat flux [*Jean-Baptiste et al.*, 1998], and the observed heat flow measurements are consistent with fluid flow from the ridge flank toward the ridge axis [*Lucazeau et al.*, 2006]. The magnetic anomaly observed at the Lucky Strike segment is axis parallel, and a low magnetization anomaly underneath the Lucky Strike hydrothermal field can be interpreted as demagnetization of the rocks by focalized hydrothermal flow [*Miranda et al.*, 2005].

3. The SISMOMAR Segment-Scale Seismic Tomography Experiment

[11] The June 2005 SISMOMAR experiment was carried out to study the crustal structure of the Lucky Strike

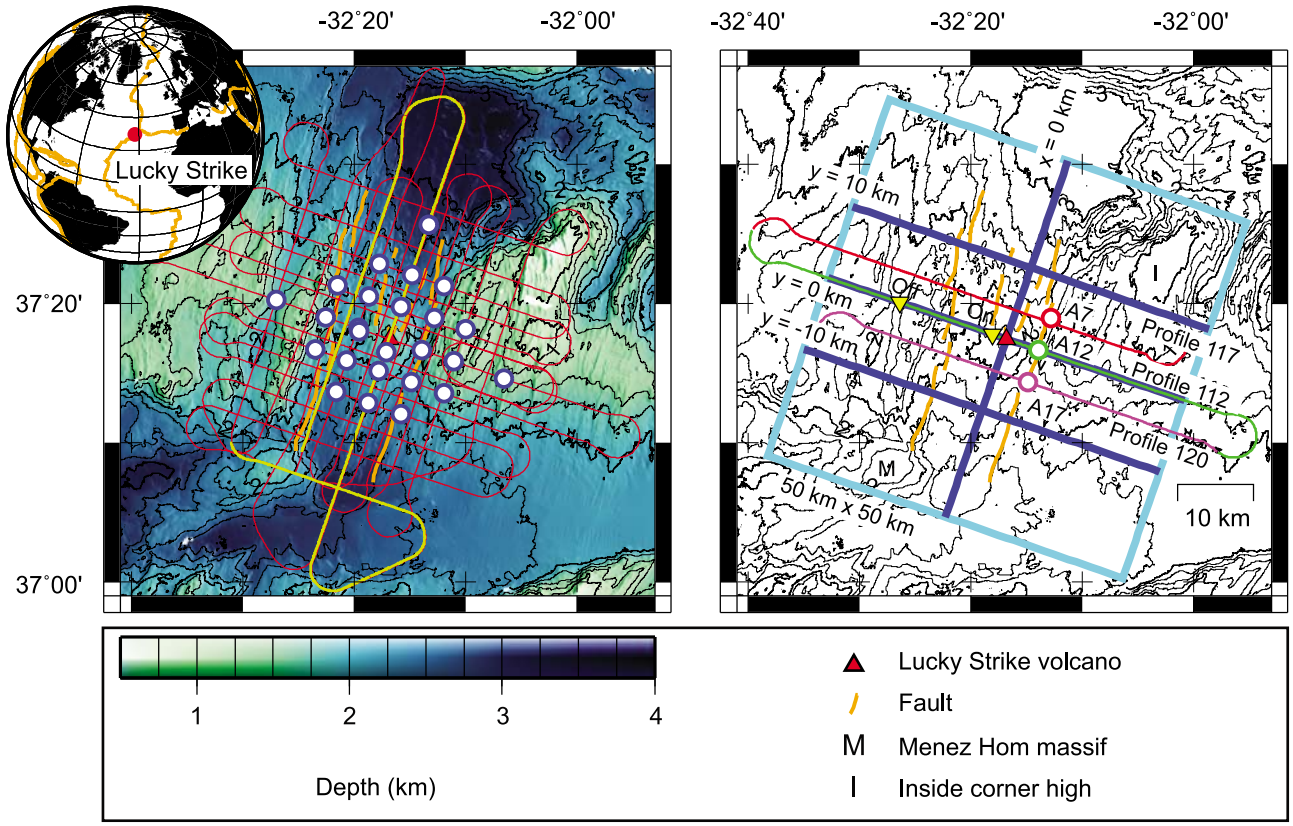

Figure 1. Overview of the SISMOMAR segment scale tomography experiment. The red triangle marks the location of the Lucky Strike volcano, and the orange lines mark the location of the median valley bounding faults and the nascent fault system cutting the Lucky Strike volcano. (left) A bathymetric map of the Lucky Strike segment. The red lines mark the 150 m spacing shot tracks, the yellow line marks the 75 m spacing shot tracks, and the blue circles mark the positions of all OBS used during the experiment. (right) The location of the measurement profiles (Figure 2) and the location of slices through the 3-D velocity model for orientation superimposed on the bathymetry. Furthermore, the position of the Menez Hom massif at the southern end of the Lucky Strike segment and the inside corner high at the northern segment end are shown. The inset shows the global position of the Lucky Strike Segment on the MAR. The global plate boundaries are marked as orange lines [*Müller et al.*, 1997].

segment using active and passive seismic methods onboard the French research vessel *L'Atalante*. The experiment consisted of seismic reflection, refraction, microearthquake, and seafloor compliance measurements. The study also included ship-based bathymetry, gravity, and magnetic measurements. Preliminary analysis of the Lucky Strike seismic reflection data revealed an axial melt lens reflector and faults that continue to at least the depth of the reflector [*Singh et al.*, 2006; *Combier*, 2007; *Dusunur et al.*, 2009].

[12] A segment scale 3-D refraction experiment consisted of a 50 × 50 km grid of sea surface air gun shots to a 32 × 26 km grid of 25 OBS, centered on the Lucky Strike volcano (Figure 1). The OBSs continuously measured seafloor motions and pressure variations using a geophone and a hydrophone. There were 25 seismic lines, with a shot spacing of 150 m, and three with a shot spacing of 75 m. The shots were triggered using GPS, and distances were relative to the shot line. The next shot position was estimated using along-profile distance, and the across-profile position of the ship was not taken into account. Thirteen lines were aligned along axis and 15 across axis, with an average line spacing of 2 km. A total of 10,403 shots were fired. There were three different types of OBS: (1) 19 instruments using a 2 Hz vertical geophone and hydrophone with a 4 ms sampling interval, (2) three instruments using a 4.5 Hz three-component geophone and hydrophone with a 10 ms sampling interval, and (3) two instruments using a broadband three-component seismometer with a 25 ms sampling interval. The gun array was 8410 cubic inches for the 150 m shot spacing and 5658 cubic inches for the 75 m shot spacing lines. The array was tuned to generate a single bubble pulse [*Avedik et al.*, 1993, 1996]. The strongest arrivals registered by the instruments are direct (water wave), Pg, and PmP phases. Seismic phases were identified based on the offset range, moveout, and frequency content of the observed arrival as well as tentative traveltime modeling of first arrivals and subsequently later arrivals. Figure 2 shows record sections and traveltime picks for three across-axis profiles. The northern and southern profiles (profiles 117 and 120) show prominent Pg and weak

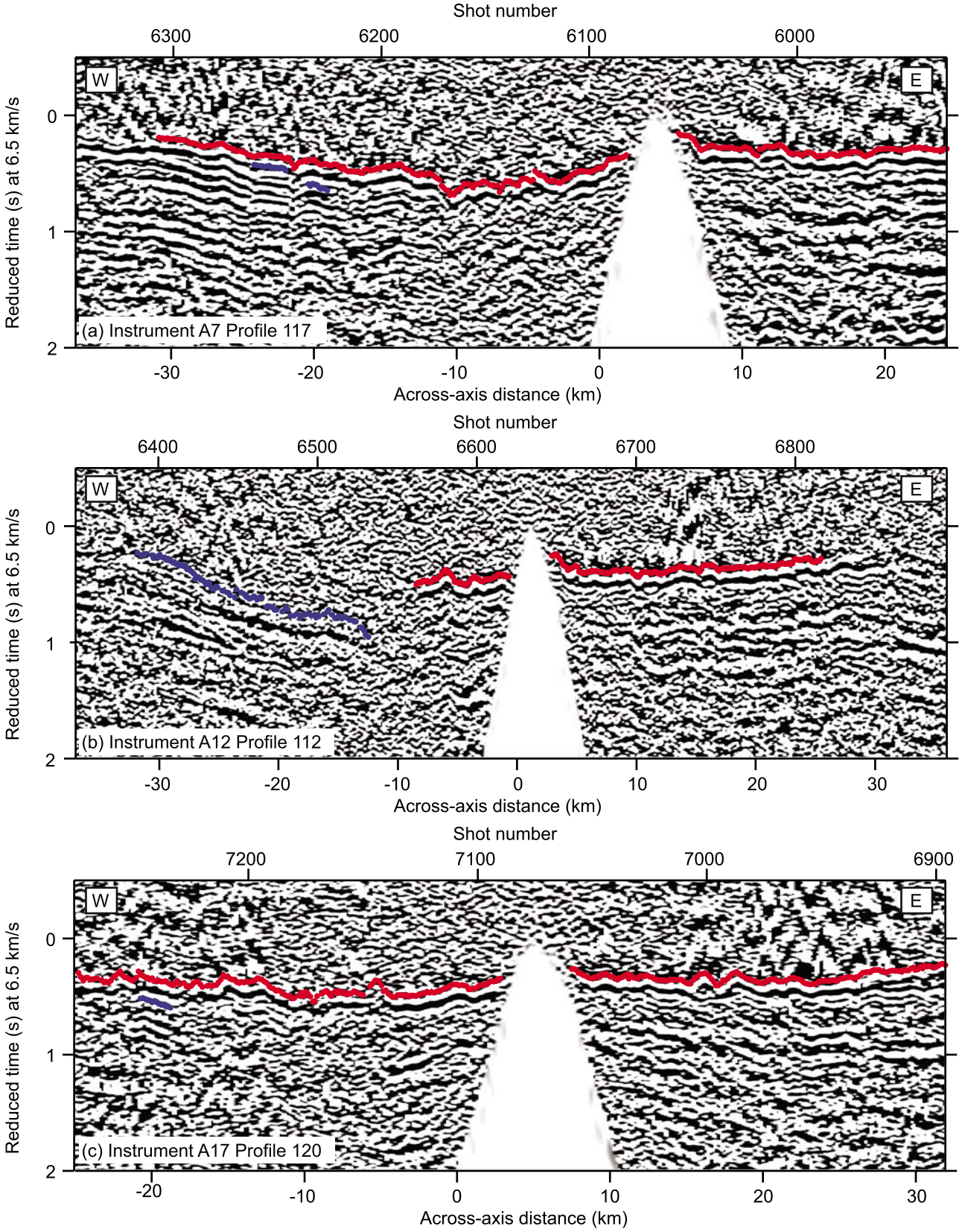
Shot number
6300
6200
6100
6000
W
E
Reduced time (s) at 6.5 km/s
0
1
2
(a) Instrument A7 Profile 117
-30
-20
-10
0
10
20
Across-axis distance (km)
Shot number
6400
6500
6600
6700
6800
W
E
Reduced time (s) at 6.5 km/s
0
1
2
(b) Instrument A12 Profile 112
-30
-20
-10
0
10
20
30
Across-axis distance (km)
Shot number
7200
7100
7000
6900
W
E
Reduced time (s) at 6.5 km/s
0
1
2
(c) Instrument A17 Profile 120
-20
-10
0
10
20
30
Across-axis distance (km)

Figure 2

PmP arrivals, whereas the central profile (profile 112) shows weaker Pg arrivals and a very prominent PmP event. Overall, Pg arrivals are observable to a maximum source-receiver offset of about 35 km and PmP arrivals to 40 km.

4. Data Processing

[13] We used three steps to estimate the 3-D subsurface velocity models: (1) we first determined the OBS and shotpoint positions, and then picked the traveltimes of seismic waves and their uncertainties; (2) we determined the model using a traveltime inversion scheme [*Hobro*, 1999; *Hobro et al.*, 2003]; and (3) we finally analyzed the model reliability.

[14] The shot position was corrected using the differential GPS position of the ship, the heading of the ship, and the distance to the center of the airgun array. The OBSs were relocated by searching for the instrument position and water column velocity that minimize the misfit between the observed and calculated traveltimes for direct water wave arrivals. This approach is similar to that used by *Creager and Dorman* [1982] and *Bazin et al.* [2001]. Before picking the traveltimes, the seismic data were corrected for the OBS clock drifts using GPS time stamps at the beginning and end of each deployment and a linear time correction. Next, we manually picked the traveltimes for 175,257 Pg and 20,028 PmP arrivals. Linear time-invariant frequency filtering was applied to the data before traveltime picking. Time delays introduced by filter during the picking process were compensated by shifting the picks to the unfiltered first break. The picked traveltimes were corrected for the time delay between the trigger signal of the air gun control and the actual airgun release. This delay was between 21 and 56 ms depending on the source configuration and was estimated using pressure sensors mounted on the airguns themselves. A third correction of approximately 7 ms was applied to correct for causal filters within the OBS digitizer. These corrected traveltimes were used as input for the traveltime inversion scheme.

[15] We identified five sources of uncertainty for the traveltime estimate: the uncertainty related to the shot location ($\Delta t_{\mathrm{Shot}} \approx 3$ ms), the uncertainty related to the OBS location ($\Delta t_{\mathrm{OBS}} \approx 2$ ms), the uncertainty related to the bathymetry ($\Delta t_{\mathrm{Bat}} \approx 16$ ms), the uncertainty related to seismic ray tracing ($\Delta t_{\mathrm{Ray}} \approx 10$ ms), and the uncertainty of the traveltime picks themselves ($\Delta t_{\mathrm{Pick}} \approx \mathrm{n} \times 16$ ms). The shot location uncertainty is caused by the difference between heading and course of the ship. Shot location during the turns of the vessel is less precise than during linear profiles; this effect was not taken into consideration in the uncertainty estimation. The OBS location uncertainty was based on the misfit of the OBS relocation. It is variable from one instrument to another. The uncertainty related to the bathymetry is related to the smoothing of the seafloor during the inversion process, which is necessary to avoid artifacts due to abrupt changes of bathymetry. The uncertainty related to ray tracing is caused by limitations of the ray-tracing algorithm and the unknown velocity distribution in the water column. The pick uncertainty was estimated by comparing picks along crossing seismic profiles, with the average difference between those picks treated as pick uncertainty, which is then multiplied by a factor of n that depends on the signal-to-noise ratio of the data at the pick [*Zelt and Forsyth*, 1994]. We estimate the overall uncertainty as the square root of the sum of the individual squared uncertainties.

[16] The mean overall uncertainties are 31 ms for Pg and 34 ms for PmP. The estimated uncertainties varied between 23 and 122 ms. While both signal and noise energy decrease with source-receiver distance, the observed signal-to-noise ratio does not systematically decrease with increasing source-receiver distance. Furthermore, the signal-to-noise ratio is lower on profiles with 75 m shot spacing. This implies that both the noise and the shot energy are created by the source and ship. Overall, the signal-to-noise ratio varies between 0.5 and 20.

[17] We calculated subsurface velocity models using the Jive3D seismic traveltime tomography software [*Hobro*, 1999; *Hobro et al.*, 2003]. The algorithm describes the subsurface velocity distribution using a regular grid of velocity nodes and the interfaces using a regular grid of depth nodes. The crustal velocity grid is limited by the seafloor and the Moho. The depth of the seafloor is determined from bathymetric measurements, and the depth of the Moho is treated independent of the seafloor. To minimize the computational overhead, we therefore chose the node spacing to be as coarse as possible without significantly increasing the data misfit. For this study, a node spacing of 2 km horizontally and 0.4 km vertically was sufficient to accurately reproduce the traveltime measurements. Our model covered a total area of 70 km $\times$ 70 km and extends to a depth of 14 km; it is discretized using a grid of 40 $\times$ 40 $\times$ 37 nodes for the velocity model and a grid of 151 $\times$ 151 nodes for the interface model.

[18] The program uses a ray shooting approach to calculate synthetic traveltimes between points. The model param-

Figure 2. Example record sections for the SISMOMAR segment scale tomography experiment. The red lines on the profiles mark the picked Pg traveltimes, and the blue lines mark the picked PmP traveltimes. The vertical axis shows traveltime after the application of a linear moveout correction with a moveout velocity of 6.5 km/s and a correction for the seafloor depth. The correction for the seafloor depth is based on the traveltime to the seafloor assuming a constant velocity in the water column and vertical raypaths which, while crude, noticeably improves the image. The profiles run directly across the instrument. The seismic data shown here were recorded using the hydrophone channel with a 10 ms sampling interval. To enhance the image, we applied a band-pass filter with cutoff frequencies of 1.5 and 36 Hz and a passband between 3 and 12 Hz, a Wiener predictive error filter [*Buttkus*, 2000], and a moving average filter (trace mixing). The direct water wave arrivals have been muted (white area). The seismic data are strongly filtered to enhance the image; these images were not used for traveltime picking. The locations of the profiles are shown in Figure 1. Profile 117 runs north of the volcano, profile 112 runs directly across the volcano, and profile 120 runs south of the volcano.

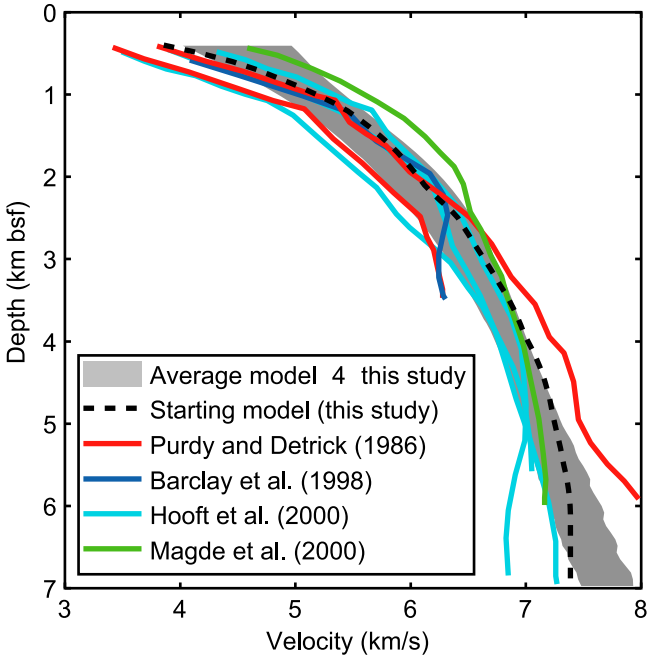

Figure 3. Comparison of different velocity depth distributions along the MAR. The starting model for our inversions was derived by averaging and smoothing the velocity depth distributions shown here. For reference the gray area in the background corresponds to the average velocity depth distribution for the best fitting velocity model 4. The width of the area corresponds to two standard deviations.

eters, in this case the B spline coefficients for the velocities and the interface positions, are then iteratively updated using a conjugate gradient scheme to minimize the difference between the calculated and observed traveltimes. For most geophysical problems an infinite number of equivalent models exist that fit the data equally well. To reduce the number of possible models, one commonly introduces prior information about the model parameters or applies additional constraints to the model structure (e.g., smoothness) in the cost function Φ.

$$\Phi = \underbrace{e^T \mathcal{W}^T \mathcal{W} e}_{\Phi_d} + \lambda \underbrace{\left(\lambda_V \|\mathcal{L}_V(\mathbf{m})\|^2 + \lambda_S \|\mathcal{L}_S(\mathbf{m})\|^2 \right)}_{\Phi_m}. \quad (1)$$

Here, the data norm Φ_d is the weighted misfit, where e stands for the difference between observed and calculated traveltimes and $\mathcal{W}$ contains the uncertainty for each traveltime pick. By changing the traveltime uncertainty for each pick preferential weighting can be applied to certain picks, e.g., Pg traveltimes can be assigned a smaller uncertainty than PmP traveltimes. The first term of the model norm Φ_m describes the smoothing of the velocity parameters, and the second the smoothing of the interface parameters. λ_V and λ_S are regularization parameters, which control the relative influence of the velocity and interface part of the model norm in the cost function, which can be used to introduce prior knowledge about subsurface velocities into the inversion. λ_V and λ_S are further split to apply preferentially weighting in different directions of the model. $\mathcal{L}$ is a linear operator, which measures a differential property of the model. Jive3D uses the Laplace operator, which is equivalent to imposing a smoothness constraint [*Constable et al.*, 1987; *deGroot Hedlin and Constable*, 1990]. The overall influence of the smoothness terms is controlled by the regularization parameter λ, which is chosen following a jumping strategy [*Shaw and Orcutt*, 1985]. At the beginning of the inversion the regularization parameter is large and only long wavelength variations are allowed in the model. As the inversion progresses and the regularization parameter is decreased, small structures gradually develop in the model.

[19] To correctly interpret a velocity model, its resolution must be assessed. In this study we applied two measures for

Table 1. Inversion Parameters and Traveltime Misfit Associated With the Final Models[a]

log(λ)	log(λ_{Vz})	log(λ_S)	Phase	χ^2	RMS (ms)	N
			Model 1: Constant Crustal Thickness			
−8	−1	0	Pg	1.2	35	(167862/175257) = 95%
			PmP	2.8	57	(13798/20028) = 69%
			Model 2: Constant Moho Depth			
−7.5	−1	0	Pg	1.1	32	(168124/175257) = 95%
			PmP	1.9	45	(16213/20028) = 80%
			Model 3: Strong Moho Smoothing			
−7	−2	1	Pg	1.1	33	(169356/175257) = 96%
			PmP	1.6	42	(17639/20028) = 88%
			Model 4: Weak Moho Smoothing			
−7.5	−1	0	Pg	1.1	32	(170149/175257) = 97%
			PmP	1.4	39	(16058/20028) = 80%
			Model 5: Velocity <7.3 km/s			
−8	−1	0	Pg	1.2	33	(169868/175257) = 96%
			PmP	1.6	41	(16716/20028) = 83%
			Model 6: No Moho			
−8	−1	0	Pg	1.1	32	(172038/175257) = 98%

[a]The variable λ is the regularization parameter at termination of the inversion; λ_{Vz} specifies the preferential weighting of velocity smoothing in z direction relative to λ; λ_S specifies the weighting of smoothing of the interface parameters relative to λ of the interface parameters; χ^2 denotes the misfit normalized by the pick uncertainty and RMS the root mean square of traveltime residuals; N stands for the ray success rate, the number of traveltimes that can be traced successfully using the corresponding velocity model; Pg denotes crustal turning waves, and PmP denotes reflections from the crust-mantle boundary.

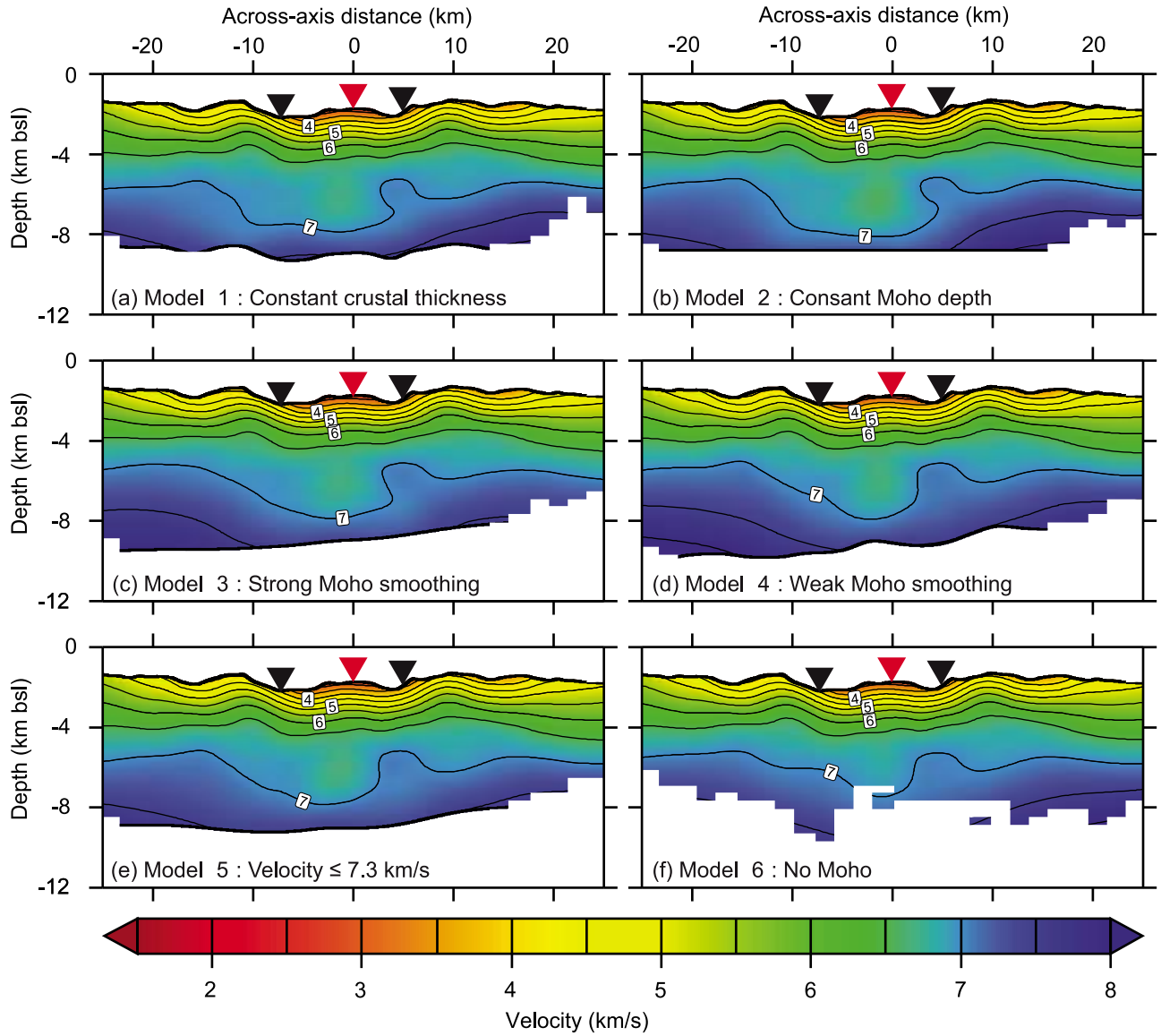

Figure 4. Comparison of different velocity models for our traveltime observations. The slices shown here run orthogonal to the ridge axis at an along-axis distance of 0 km (Figure 1). The upper interface corresponds to the seafloor and the lower interface to the crust-mantle boundary or the Mohorovièić discontinuity (Moho). (a) Model 1 has a constant crustal thickness. (b) Model 2 has a constant depth below sea level crust-mantle boundary. (c) Model 3 was derived by preferentially smoothing the interface nodes with respect to the depth nodes. (d) Model 4 was derived using equal smoothing for the velocity and interface nodes. (e) Model 5 is similar to model 4, with velocities clipped at 7.3 km/s. (f) Model 6 was derived using crustal turning rays only. The vertical exaggeration is 2:1. The black triangles mark the location of the eastern and western bounding faults at the surface. The red triangle indicates the position of the Lucky Strike volcano.

the model resolution, the hit count (or ray density) [*Kissling*, 1988] and the resolvability [*Lévêque et al.*, 1993; *Zelt*, 1998, 1999] (Appendix A). Calculation of the a posteriori covariance matrix was not feasible due to the size of the inverse problem. The first measure of model resolution, the hit count, is based on counting the number of rays hitting every velocity cell. We choose an arbitrary cutoff of 100 crossing raypaths in a cell, below which velocity values are considered unreliable. The second measure of a model's reliability is the resolvability or averaged semblance [*Zelt*, 1998], which we calculated using checkerboard tests.

5. Results

5.1. Inversion Strategy

[20] To interpret the seismic data (see Figure 2 for examples of our seismic data), we estimate crustal velocity models. We first constructed a 1-D starting model (Figure 3)

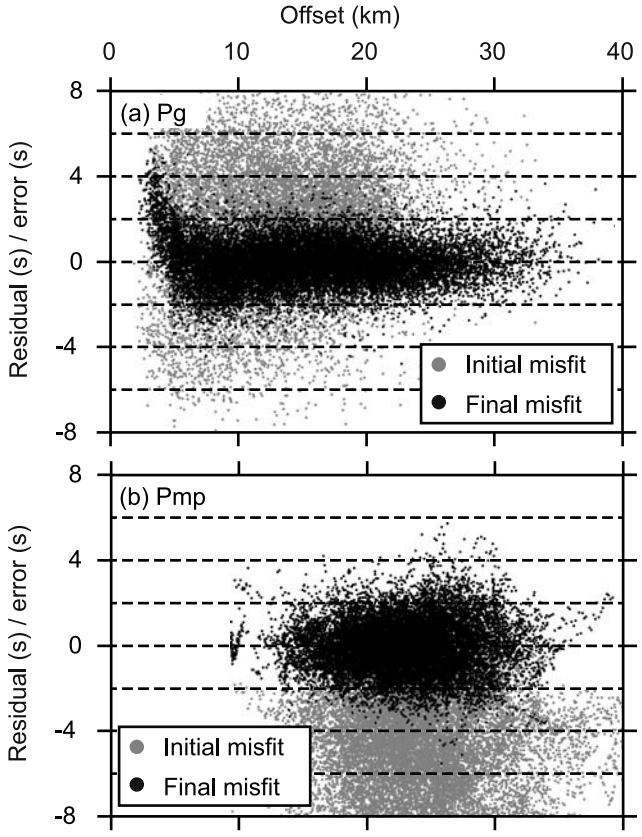

Figure 5. Comparison of normalized residuals for the starting model and the final model 4. Normalized residuals for (a) crustal turning rays (Pg) and (b) reflections from the crust-mantle boundary (PmP). For clarity, only 10% of the Pg residuals are plotted. At conversion, 68% or 95% of the normalized residuals should lie within one or two standard deviations, respectively.

by averaging over crustal velocity models obtained for other MAR segments [*Purdy and Detrick*, 1986; *Barclay et al.*, 1998; *Hooft et al.*, 2000; *Magde et al.*, 2000]. The MAR velocity-depth profiles shown here are a small subset of those available, but illustrate the variability of velocities typically observed along the northern MAR south of the Azores hot spot. The velocity-depth profiles from the OH-1 segment were chosen because of the segment's similarity to the Lucky Strike segment. The MAR velocity-depth profiles all have a similar structure: seismic velocities increase rapidly in the upper crust (the first 1 to 2 km below seafloor (bsf)) and increase more gradually at greater depth except for the velocity profile by *Purdy and Detrick* [1986], which indicates a steeper velocity gradient below a depth of 3 km bsf. While the overall structure is similar, the absolute velocities can vary by as much as 1 km/s at a given depth bsf between different locations. We hung the 1-D starting model from the seafloor to construct a 3-D starting model for all inversions. Our tests show that the final model depends only weakly on the starting model.

[21] Pg waves are observed in the top few kilometers of crust because the velocity gradient there is steep. Deeper in the crust, the velocity gradient flattens and very few Pg waves are observed. Therefore, PmP reflections are needed to constrain both the lower crustal velocities and the structure of the Moho. The Moho is the effective lower boundary of our velocity model because no upper mantle turning waves were observed. By solving for seismic velocity and interface position using the same data, one risks mapping velocity variations to changes of the interface depth and vice versa: this is known as the velocity-depth trade off. An increase in the modeled velocity decreases the traveltime to cross a given distance and, consequently, an overestimate of the velocity causes an overestimate of the interface depth. The choice of the regularization between the velocity and interface parameter is therefore crucial. We used six different combinations of regularization parameters and prior information to test the effect of this choice. The regularization parameters are summarized in Table 1. Slices through the velocity models are shown in Figure 4, and the final misfits are listed in Table 1.

[22] Models 1 to 5 were calculated using both Pg and PmP traveltimes, whereas model 6 used only Pg traveltimes. Models 1 and 2 are "end-member" models with model 1 a constant thickness crust and model 2 a constant depth below sea level (bsl) Moho. Those simplifying assumptions reduce the number of free parameters, but cause a larger misfit for the PmP phase (Table 1). In model 4 the smoothing of velocity and interface components had equal weight, whereas in model 3 the interface smoothing had additional weight. Both models 3 and 4 show velocities higher than 7.3 km/s in the lower crust around the model edges (Figure 4), but gabbro velocities do not exceed 7.3 km/s [*Christensen*, 1979]. Higher lower crustal compressional velocities can be explained through an elevated Olivine content [*Miller and Christensen*, 1997]. Limiting the velocity variability is an effective way to reduce the nonuniqueness, the number of equivalent solutions, of the inverse problem. In model 5 we tried to limit the upper bound for the crustal velocities to 7.3 km/s. First, we clipped the velocities in model 4 at 7.3 km/s; then we optimized only the position of the Moho using PmP traveltimes. This is equivalent to an inversion for a floating reflector [*Zelt*, 1999]. Finally, we optimized the velocity distribution while keeping the interface positions fixed. This approach forces the inversion to minimize lower crustal velocity variations. These additional constraints cause model 5 to have slower lower crustal velocities and a shallower Moho than models 3 and 4.

[23] The quality of a model manifests itself in its ability to reproduce observations to within the associated measurement uncertainties. Traveltime residuals, the difference between the observed and the synthetic traveltimes, are one measure of the model quality (Figure 5). Assuming our observations do not contain any systematic errors and our estimate of uncertainty is correct, the normalized misfit of the final model should be equal to unity and all traveltime residuals should follow a normal (Gaussian) distribution.

[24] The termination condition chosen for the inversions is a combined Pg and PmP χ^2 smaller than or equal to 1.2 and a combined ray success rate equal to or above 95% (i.e., more than 95% of the observed Pg and PmP arrivals were modeled successfully). This criterion was met for models 3, 4, and 5, but not for models 1 and 2 which are shown for comparison only. Model 6 meets the criterion for the Pg phase only, since the PmP phase was not included in the inversion. All six velocity models are well constrained in

seismic layer 2B and the upper part of seismic layer 3, where they are dominated by Pg observations (Figure 4). The velocity inside seismic layer 2A is less well constrained. Because of the presence of seismic layer 2A the moveout of the seismic arrivals is smaller close to the OBS than at larger offsets. However, most seismic layer 2A arrivals arrive after the water wave and have not been included in the inversion. The similarity of the models in layer 2B and the upper part of layer 3 indicates that PmP traveltimes have only a minor influence on the near-surface model, but dominate the region close to the Moho. The velocity structure in the lower crust can vary by as much as 0.5 km/s depending on the constraints imposed on the Moho, but the velocity above a depth of approximately 7 km bsl (5.5 km bsf) does not vary much with changes of the Moho.

[25] For all velocity models the RMS misfit is <35 ms and the normalized misfit is close to unity for the Pg phase. More than 95% of the observed traveltimes are modeled successfully (Table 1). However, for PmP reflections the RMS misfit is larger and the percentage of successfully traced rays is much lower (80%). Overall, the number of PmP observations is approximately a magnitude smaller than the number of Pg observations. Even if the PmP misfit is large, the overall misfit can still be minimized. A possible reason for the low ray success rate associated with PmP reflections is a problem with modeling large offset reflected phases. The point where reflections become turning rays is very difficult to model, as it requires precise knowledge of the velocity and interface structure. A slight mislocation of the interface or slightly wrong velocity profile can lead to rays no longer being traced successfully, as the modeled ray does not reach the interface or is reflected in the wrong direction. Once far offset ray tracing fails, there is no way back, as there are no observable turning rays from deeper parts of the model to stabilize the inversion. This is a limitation of the ray shooting method as opposed to ray bending or minimum time methods. On the other hand, the failure to reproduce far-offset observations might be related to the fact that those observations are modeled as reflections, which might be invalid. There is evidence that the Moho does not necessarily constitute a step change in velocity, but can correspond to a transition zone, whose thickness can vary by hundreds of meters [*Jousselin and Nicolas*, 2000].

5.2. Crust-Mantle Boundary

[26] A comparison of the different models allows us to assess which features are required by the data and which features are artifacts of the inversion. For the Moho, we analyze only those features common to the three models that allowed this interface to vary (models 3 to 5) to avoid interpreting unconstrained properties. The Moho depths (Moho depths bsl) and crustal thicknesses (Moho depths bsf) for models 3 to 5 are shown in Figure 6. We show map views of the Moho reflector both as a function of depth from the sea surface and as a function of depth beneath the seafloor, i.e., crustal thickness. Smoothing is applied to the Moho depth bsl; smoothing the crustal thickness is not offered by the tomography program. Since the inversion tries to minimize structure with respect to a flat horizon such as the sea surface, the smoothness constraint in the inversion can map into apparent structure in the thickness plots. Therefore, the depth from sea surface plots helps to show what features are indeed required by the data and which ones are influenced by the smoothing. The data are clipped to show only the grid elements with observed PmP reflections. While the exact distribution of reflection points varies for the different velocity and interface models, the PmP observations constrain approximately the same area in the three models. The interface is reasonably well sampled between −15 and 15 km across axis and −10 to 15 km along axis, except to the southwest, where less PmP reflections were observed.

[27] In all of the models for which the Moho depth was inverted, the Moho is deepest in the southwest and shallowest in the northeast. The crust is thickest to the west and thin toward the segment ends. Along the ridge axis, the crust is 5–6 km thick north and south of the volcano and 7–7.5 km thick beneath the volcano. The crust is thickest (7.25–8.25 km) west of the volcano. The biggest difference between the models is the Moho depth beneath the volcano. While model 4 shows an uplift of the Moho depth underneath the volcano (Figure 6b, 0 km across axis and −5 km along axis), models 3 and 5 have a smoother Moho depth, which shows no uplift underneath the volcano. Overall, the difference between the different Moho depths and crustal thickness estimates is less than 1 km.

[28] The six velocity models are nearly identical above a depth of 7 km bsl (5.5 km bsf) (Figure 4). The largest differences between models occur in the lower crust at the eastern and western edges of the model; the variability in the along-axis direction (not shown) is generally smaller than in the across-axis direction. All six models show a lower crustal velocity increase away from the segment center and a lower crustal low-velocity region centered at about 0 km along axis and −5 km across axis. We choose model 4 for further analysis. The main reason for selecting model 4 over model 3 or 5 is that less prior information about the subsurface velocities was introduced into the inversion. However, lower crustal velocities in model 4 are greater than 7.3 km/s, which requires the presence of olivine-rich peridotite. On the contrary, model 5 shows lower crustal velocities consistent with pure gabbro. The discrepancy between the different models is caused by the velocity uncertainty directly above the Moho.

[29] To assess the quality of our velocity models, we compare the Bouguer gravity anomaly predicted by our velocity model 5 to the Bouguer anomaly predicted by a constant crustal thickness model. To estimate the sea surface gravity, we first converted our seismic velocities to density using the relation by *Carlson and Raskin* [1984] for the crust and assumed a mantle density of 3.3 Mg m^{-3} [*Escartín et al.*, 2001]. Next, we estimated the gravitational attraction using the method of rectangular parallelepipeds [*Banerjee and Das Gupta*, 1977]. The external boundary of our velocity model was extended ~3000 km in each horizontal direction to avoid edge effects assuming a lateral continuation of our density model. The gravitational attraction for all parallelepipeds was integrated and subtracted from the free-air gravity anomaly observed during the SISMOMAR cruise. The residual gravity between our model and the free air gravity is the combined effect of the lower crustal velocity and thickness variation not well constrained by our velocity model, and the variability in the

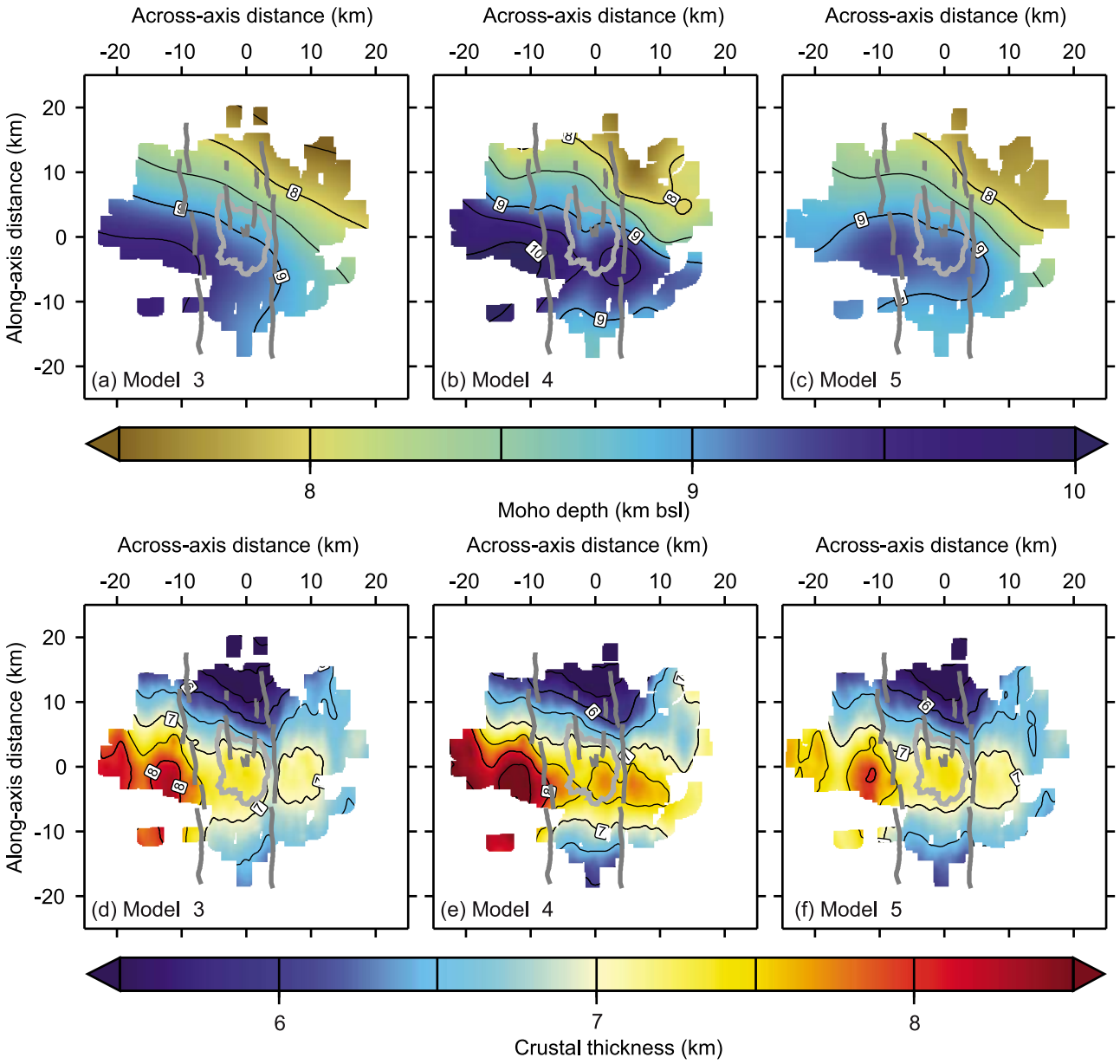

Figure 6. Depth to the crust-mantle boundary and crustal thickness for the models 3, 4, and 5 shown in Figure 4. The area of the images shown here corresponds to the 50 km × 50 km area shown in Figure 1. Grid cells without any reflection points have been masked. The light gray line marks the position of the volcano's 2 km depth contour and the dark gray lines the position of major faults. (a–c) Depth beneath the sea surface. (d–f) Crustal thickness (depth beneath the seafloor).

mantle. For comparison with the gravity predicted by our velocity model, we evaluated the Bouguer anomaly for a density model with a crustal thickness of 6 km, a crustal density of 2.7 Mg m^{-3}, and a mantle density of 3.3 Mg m^{-3} [*Escartín et al.*, 2001]. No thermal correction was applied in either case.

[30] The free-air gravity anomaly observed during the SISMOMAR cruise (Figure 7a) is dominated by the bathymetry. Applying a constant crustal thickness Bouguer correction removes the effect of bathymetry and shows a Bouguer bull's-eye anomaly (Figure 7b) located in the same place as the anomaly observed by *Escartín et al.* [2001]. This anomaly has previously been interpreted as evidence for elevated temperatures or partial melt in the crust/mantle or crustal thickness variations. Using our crustal velocity model to compensate for density and thickness variations removes the Bouguer bull's-eye anomaly (Figure 7c). While our density model compensates the gravity increase toward the northern segment end, we still observe a gravity increase toward the southern segment end consistent with an overestimate of crustal thickness in our velocity model. The observed Bouguer bull's-eye anomaly can be explained by crustal density and thickness variations alone and does not require the presence of partial melt or elevated temperatures in the mantle. Larger scale variations in the mantle are likely, but cannot be imaged because of the spatial limi-

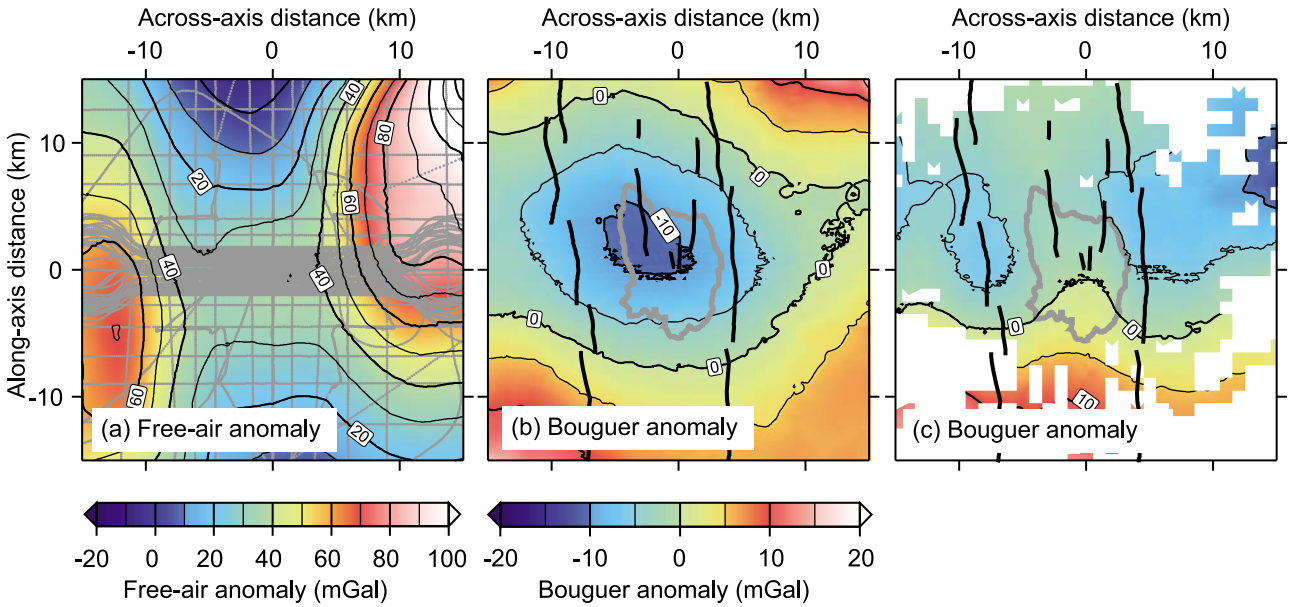

Figure 7. Gravity anomalies around the Lucky Strike volcano. (a) Free-air gravity anomaly measured during the SISMOMAR cruise. The gray points show the measurements. (b) Bouguer gravity anomaly for a density model with a constant crustal thickness of 6 km, a crustal density of 2.7 Mg m^{-3}, and a mantle density of 3.3 Mg m^{-3}. (c) Bouguer gravity anomaly based on our crustal velocity model 5 converted to density using the relationship by *Carlson and Raskin* [1984]. The black lines mark the location of major fault systems and the gray line the outline of the Lucky Strike volcano.

tations of the experiment. Most importantly, the gravity predicted by our velocity model is consistent with the free-air gravity observations during the SISMOMAR survey.

5.3. Three-Dimensional Velocity Model

[31] The crustal structure of the Lucky Strike segment is characterized by tectonics and focused magmatism at the segment center. The variability seen at the seafloor cannot be explained using simple one- or two-dimensional approximations, but shows significant variations in three dimensions. Our 3-D velocity model images spatial variations in seismic velocities within the ridge segment, which can then be interpreted with respect to crustal structure. A detailed analysis of the resolution of our velocity models is given in Appendix A.

[32] To illustrate the variations of the velocity model, we show both the velocity and the velocity anomaly for our preferred model (Figures 8 and 9). The velocity anomaly model is the 3-D velocity model minus its own mean velocity at each depth bsf (the 1-D mean model in Figure 3). The mean velocity is estimated by averaging over all constrained velocity nodes at a certain depth bsf.

[33] Upper crustal velocities underneath the Lucky Strike median valley are significantly lower than velocities underneath the median valley walls (Figures 8a–8f and 9). At a depth of 1 km bsf, the lowest velocities are found beneath the northwestern volcanic ridge and the Lucky Strike volcano. The lowest velocities do not coincide with the hydrothermal vent field. Velocities are low in the upper crust over the whole length of the segment (Figures 8g and 8h). With increasing depth, the amplitude of the negative velocity anomaly decreases and it has disappeared by approximately 2 km bsf (Figure 9). The across-axis limit of the region of decreased velocities coincides with the median valley bounding faults. At a depth of 1 km bsf velocities vary between 4.5 and 5 km/s inside the median valley and increase by approximately 1 km/s outside the bounding walls. Furthermore, a more gradual velocity increase with distance from the ridge axis can be observed outside the median valley.

[34] While midcrustal (2 to 3 km bsf) velocities vary little across axis (Figure 9), they decrease toward the segment ends (Figures 8g, 8h, and 9), with the lowest values found at the segment ends. The high-velocity band in the segment center extends on both sides of the ridge axis. Furthermore, the high-velocity band contains isolated zones with even higher velocities (Figure 9).

[35] Lower crustal velocities (deeper than 3 km bsf) are dominated by a region of decreased velocities that underlies the segment center melt lens reflector. This region starts at approximately 3.5 km bsf (5 km bsl) and continues to the Moho (Figures 8c, 8d, 8g, 8h, and 9). The region extends approximately 5 to 10 km away from the segment center in all directions at a depth of 5 km bsf. The velocity minimum is approximately 0.6 km/s slower than the mean velocity values at the same depth. This is a conservative velocity estimate because the inversion searches for the smoothest solution possible and because most of the information comes from seismic waves passing close by the low-velocity region, as a decrease in velocity with depth can prevent Pg rays from returning to the surface. Significantly lower velocities in a smaller volume produce similar results (Appendix A). Furthermore, the estimated velocity anomaly depends on the assumed background velocity model. Velocity models 3 and 5 show a lower amplitude velocity anomaly in the lower crust.

[36] The across-axis cross section 10 km north of the volcano (Figures 8a and 8b) is similar to the cross section

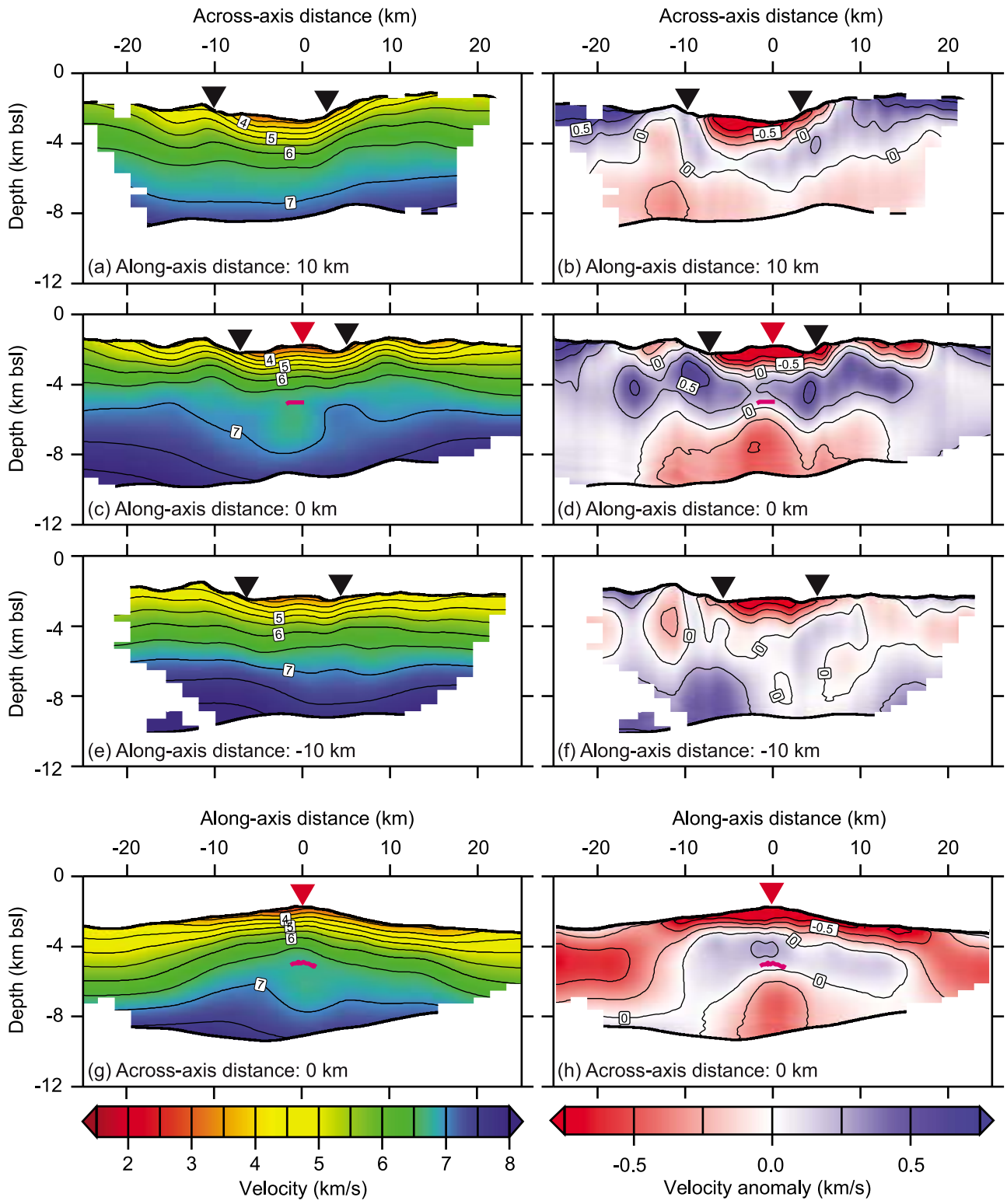

Figure 8. (left) Two-dimensional cross sections through the 3-D velocity model 4 and (right) the corresponding velocity anomaly distribution. Cross sections shown here run (a and b) 10 km north of the volcano, (c and d) across the volcano, (e and f) 10 km south of the volcano, and (g and h) along the ridge axis (Figure 1). The velocity anomaly was estimated by subtracting the average velocity profile shown in Figure 3. Cells not crossed by at least 100 rays are not shown. The black triangles mark the location of the eastern and western bounding faults at the surface. The red triangle indicates the position of the Lucky Strike volcano. The magenta lines mark the location of the axial melt lens reflection [*Singh et al.*, 2006; *Combier*, 2007]. The upper interface corresponds to the seafloor, and the lower interface corresponds to the crust-mantle boundary. The vertical exaggeration is 2:1.

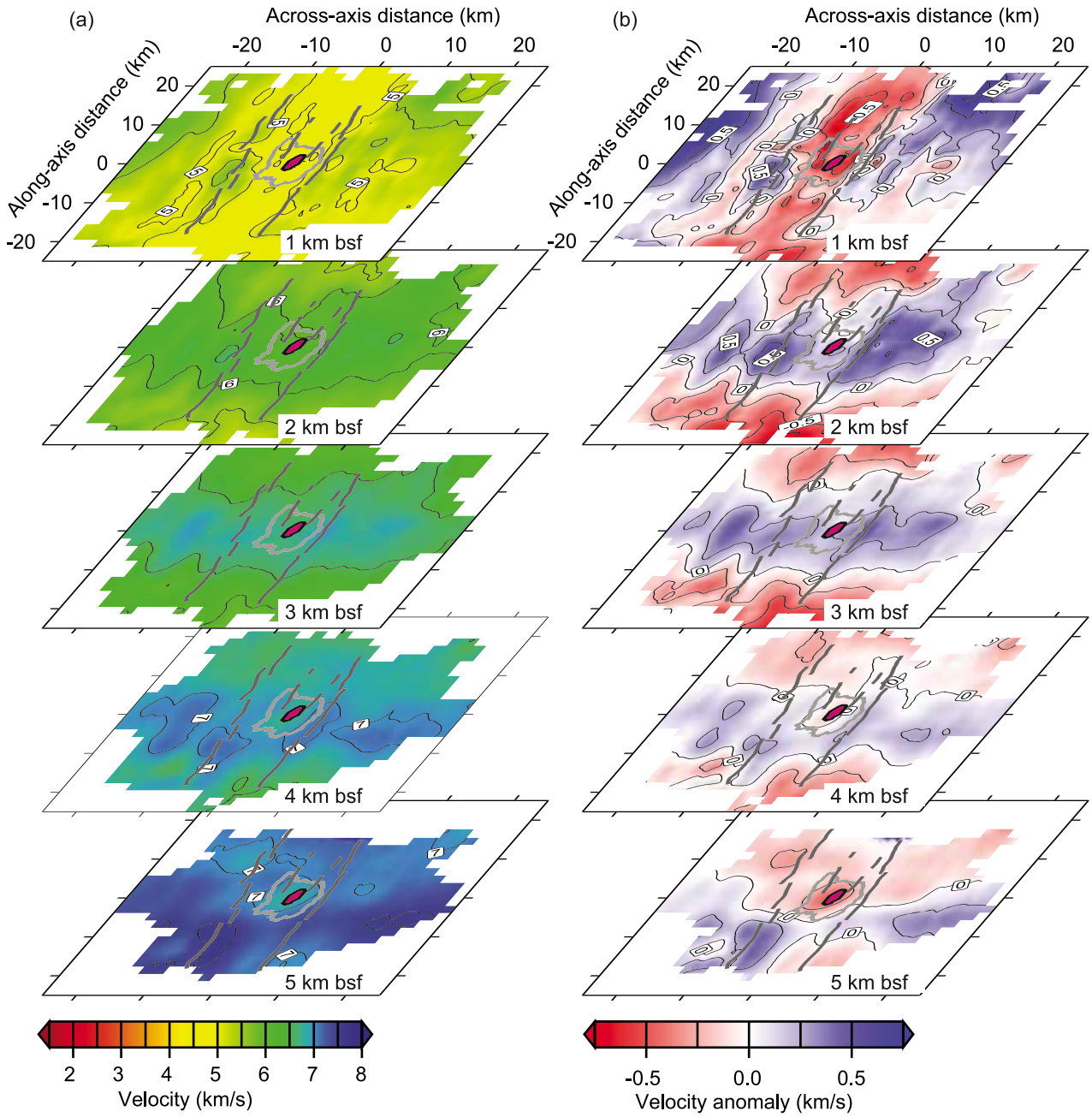

Figure 9. Lateral variation of the crustal velocity model between 1 and 5 km below the seafloor. Velocity nodes with no ray coverage have been masked. The area of the images shown here corresponds to the 50 km × 50 km area shown in Figure 1. The light gray line marks the position of the volcano's 2 km depth contour, and the dark gray lines mark the position of major faults. The magenta area shows the location of the axial melt lens reflection [*Singh et al.*, 2006; *Combier*, 2007]. (a) Seismic velocities. (b) Velocity anomaly. We calculated the velocity anomaly with respect to the mean crustal velocity model shown in Figure 3.

10 km south of the volcano (Figures 8e and 8f), but some of the features are exchanged east to west. While velocities 10 km south of the volcano are higher on the western side of the median valley, velocities 10 km north of the volcano are higher on the eastern side of the valley. Both the northern and southern cross sections show a zone of anomalously high velocities underlying a bounding fault: the eastern bounding fault for the northern section and the western bounding fault for the southern section. These high-velocity zones are in both cases on the side of the valley with the most pronounced bounding wall bathymetry, which in turn corresponds to the location of the inside corner high: to the east at the north of the segment and to the west at the south of the segment.

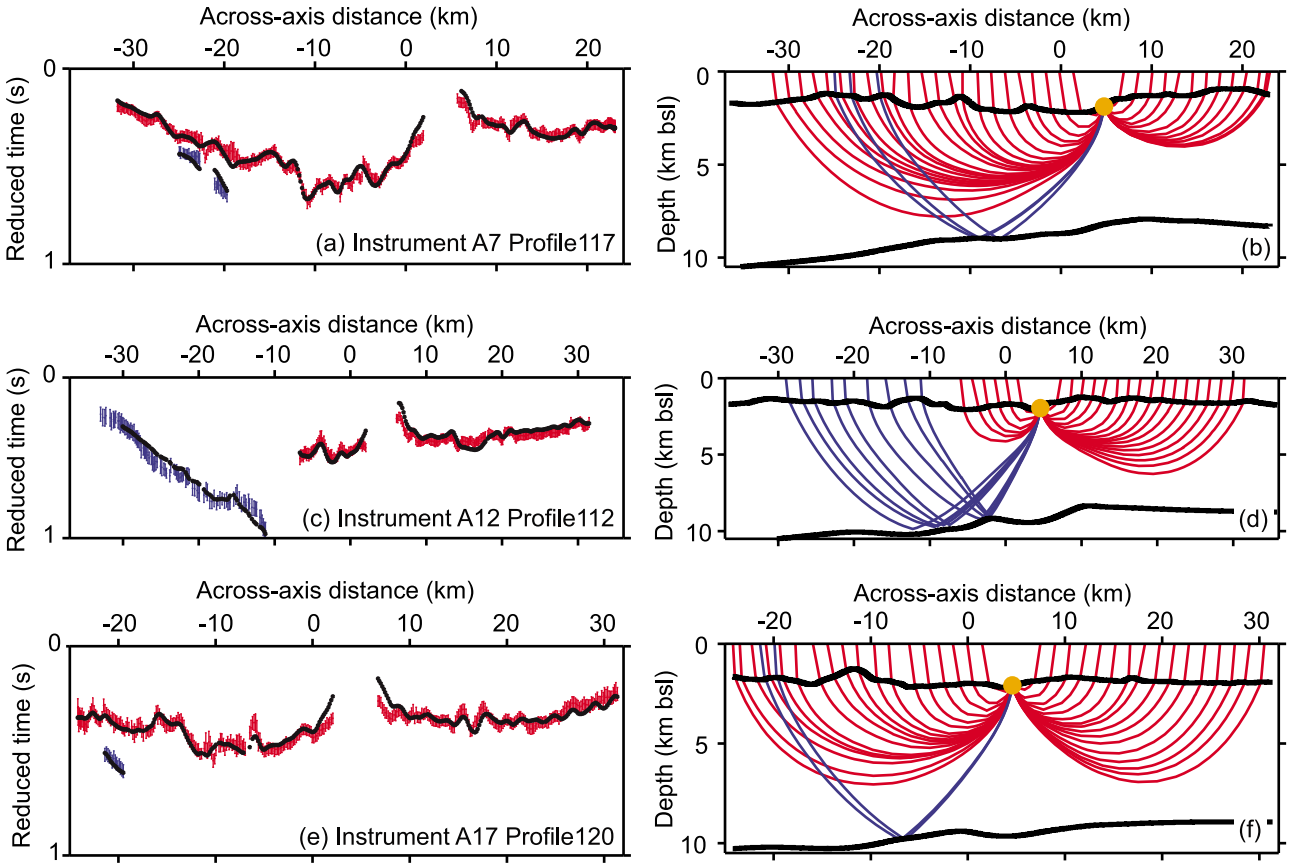

Figure 10. Synthetic and picked traveltimes and corresponding raypaths for our best fitting velocity model. (a, c, and e) The picked traveltimes and the associated traveltime uncertainties in red for Pg picks and in blue for PmP picks. The synthetic traveltimes are superimposed as a black line. The time has been reduced by applying a linear moveout correction with 6.5 km/s and a correction for the depth to the seafloor. (b, d, and f) The raypaths corresponding to the synthetic traveltimes shown here. The number of raypaths has been reduced by a factor of 10. The Pg rays are shown in red, and the PmP rays are shown in blue. The location of the OBS is marked as an orange circle. The profiles shown here correspond to the record sections shown in Figure 2. Refer to Figure 1 for the location of the profiles.

5.4. Traveltime Residuals and Azimuthal Anisotropy

[37] The distributions of the traveltime residuals can show systematic variations that are not explained by the velocity model. Figure 10 shows observed and synthetic traveltimes as well as the associated raypaths for the three record sections shown in Figure 2. For offsets smaller than 5 km, the predicted traveltimes are systematically too small (Figure 5). This misfit is possibly caused by the inversion regularization. The velocities in the uppermost crust are likely to be low and the vertical velocity gradient steep [*Hussenoeder et al.*, 2002], but they are poorly constrained by OBS refraction data. The velocities below this zone have a significantly lower velocity gradient and are much better constrained. The inversion algorithm tries to minimize the change in the velocity gradient (the model curvature) and therefore extrapolates the low-velocity gradient to shallow depth, overestimating shallow velocities. Alternatively, this trend may be related to vertical velocities being faster than horizontal velocities, since near-offset observations have a larger nonvertical component. These effects would be enhanced by the geometry of the raypaths, most of which cross the first kilometer of the crust almost vertically. Overestimating upper crustal velocities does not have a large influence on traveltimes for rays traveling almost vertically, as they spent only a very small time in the upper crust.

[38] To assure that the short-offset traveltime picks do not cause any spurious anomalies in the model, we ran an inversion in which we used only traveltime picks with offsets larger than 7 km. The difference between the bootstrap model and our best fitting model 4 is smaller than 0.25 km/s everywhere except for the near surface. In the first kilometer bsf, velocities in the bootstrap model are between 0.25 and 0.5 km/s higher than in the velocity model including the near-offset data. The difference between the velocity model including data with offsets smaller than 7 km and the velocity model derived without these data is smaller than the proposed velocity uncertainty of 0.5 km/s. Most importantly, no anomalies in our best fitting model disappear in the bootstrap model. We conclude that the short offset data, although systematically misfit by the inversion, do not deteriorate the model quality and need not be removed from the inversion.

[39] Prior work along the MAR [*Barclay et al.*, 1998; *Dunn et al.*, 2005] has shown that anisotropy of seismic

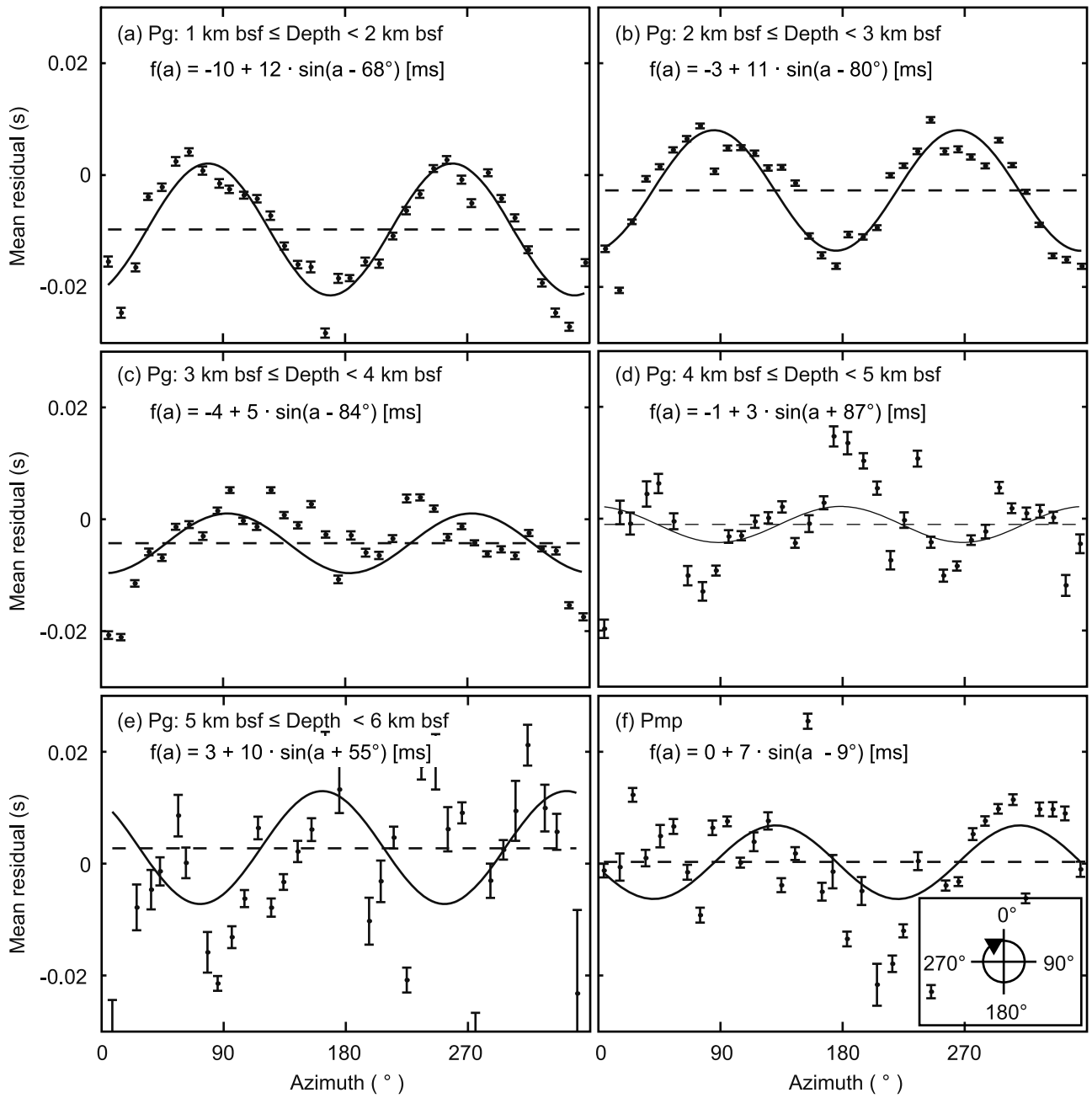

Figure 11. Average traveltime residual for all instruments averaged for (a–e) Pg picks and (f) PmP picks. The Pg residuals were averaged in 1 km wide turning depth bins between 1 and 6 km below the seafloor. The error bars show the uncertainty of the mean. The dashed line indicates the mean traveltime residual, and the solid line indicates the best fitting sinusoid corresponding to the formula above. The inset in Figure 11f illustrates the azimuths; 0° is parallel to the ridge axis (≈19°N).

velocities causes an approximately sinusoidal variation of traveltime residuals (i.e., the observed traveltimes minus the calculated traveltimes) for isotropic velocity models. A mathematically more rigorous treatment is given by *Backus* [1965]. For turning depths shallower than 4 km bsf, we observe an azimuthal variation with respect to the ridge axis (Figure 11). Below 4 km bsf, the amplitude of the best fitting sinusoid is smaller than the scatter in the data, and no evidence for azimuthal anisotropy exists. Near the surface rays traveling parallel to the ridge axis show negative residuals: the observed traveltimes are smaller than the calculated traveltimes. This means that rays travel faster along the ridge axis than predicted by our velocity model. For rays traveling orthogonal to the ridge axis the reverse applies. The upper crustal low-velocity region is therefore anisotropic, with the fast direction approximately along axis.

[40] For turning depths smaller than 3 km bsf the amplitude of the peak-to-peak variation of the residual is ~20 ms. For turning depths of 3–4 km bsf, the amplitude of the variation decreases to ~10 ms and has disappeared below a depth of 4 km. For turning depths between 1 and

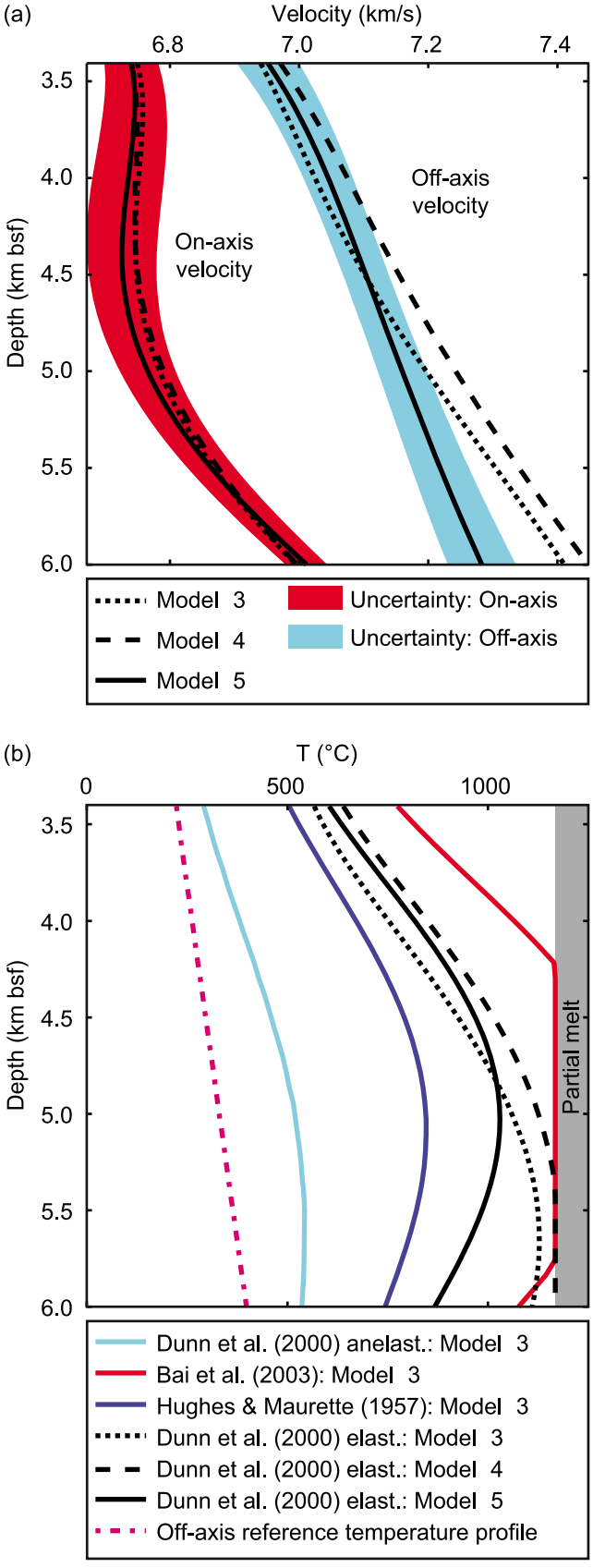

Figure 12. Estimated temperature underneath the Lucky Strike volcano. (a) Average velocity underneath the volcano on the ridge axis and 15 km west away from the ridge axis. The average velocity profiles were estimated by averaging all velocity nodes within a 4 km × 4 km area. The widths of the colored areas correspond to one standard deviation of model 5. The reference positions are marked in Figure 1. (b) Reference off-axis temperature [*Chen and Morgan*, 1990] and on-axis temperatures estimated using the velocity contrast between the two velocity profiles shown in Figure 12a and different temperature-velocity relationships [*Hughes and Maurette*, 1957; *Dunn et al.*, 2000; *Bai et al.*, 2003]. The temperatures were clipped at 1170°C, which corresponds to the approximate liquidus temperature of mid-ocean ridge basalt melt [*Sinton and Detrick*, 1992; *Perfit and Chadwick*, 1998].

2 km bsf (Figure 11a) we observe the near-offset static shift on the order of 10 ms. Examining the azimuthal variation shows that the fast direction is oriented ~0°N–10°N, which is ~10°–20° to the north away from the ridge axis.

[41] To obtain a first impression of the velocity anisotropy linked to the observed traveltime residuals, we estimate analytic traveltimes for a constant velocity gradient model. We chose the velocity gradient model that best fits our mean velocity model (Figure 3) to the observed turning depth. To explain the observed peak-to-peak variation of ~20 ms above a depth of 3 km bsf we require a velocity anisotropy of 1%–2%. Below a turning depth of 3 km bsf a velocity anisotropy <0.5% is sufficient to explain the observed traveltime residual. This anisotropy is slightly smaller than the 2%–4% observed at OH-1 [*Barclay et al.*, 1998; *Dunn et al.*, 2005].

6. Temperature and Melt Content in the Lower Crust

[42] To estimate the temperature beneath the Lucky Strike volcano and the axial magma chamber, we follow a method developed by *Dunn et al.* [2000] for the East Pacific Rise and applied to the MAR by *Canales et al.* [2000]. The procedure involves calculating coincident off-axis velocity and temperature profiles. The off-axis velocity profiles are then subtracted from the velocities on the ridge axis. Assuming that the same materials are found on and off axis, this difference can be related to a change in physical conditions like temperature, pressure, or the presence of fluids. The velocity anomaly can then be converted to a temperature anomaly using temperature-pressure relations measured in the laboratory. Adding this temperature anomaly to the off-axis temperature profile gives an estimate of the on-axis temperatures beneath the axial melt lens reflector.

[43] The first step in estimating the temperature field is to estimate the off-axis temperature. There are many, quite different, models for the subsurface temperature distribution near the MAR [*Chen and Morgan*, 1990; *Henstock et al.*, 1993; *Dusunur*, 2008]. The variability between these temperature models is approximately 300°C at 10 km from the ridge axis, which we take as the uncertainty of the background temperature model. Here, we will use the model of

Table 2. Comparison of Laboratory Measurements of Velocity-Temperature Gradients for Different Gabbro Samples[a]

Reference	Pressure	$(\partial \log V/\partial T)$
Hughes and Maurette [1957] (I)	Variable	$(-1.9 \pm 0.3) \times 10^{-4}$
Hughes and Maurette [1957] (II)	Variable	$(-1.1 \pm 0.2) \times 10^{-4}$
Christensen [1979]	$p = 0.2$ GPa	$(-8.1 \pm 0.2) \times 10^{-5}$
Bai et al. [2003]	$p = 1$ GPa	$(-2.3 \pm 0.1) \times 10^{-5}$

[a]The compressional wave velocity V is given in km/s, and the temperature is given in °C. The gradients were derived by linear regression for temperature to the laboratory data given by *Christensen* [1979] and *Bai et al.* [2003] or by bilinear regression for temperature and pressure for the data given by *Hughes and Maurette* [1957]. The data were measured for a San Marco Gabbro (I) [*Hughes and Maurette*, 1957], a hornblende gabbro (II) [*Hughes and Maurette*, 1957], and a gabbro from the MAR [*Christensen*, 1979].

Chen and Morgan [1990] at an off-axis distance of 15 km (Figure 12b), where our low-velocity anomaly has all but disappeared. We calculate 1-D mean velocity profiles for the Lucky Strike volcano and for the region 15 km west of the Lucky Strike volcano (Figure 12a). The mean velocities were estimated by averaging the velocities found in an area of 4 × 4 km. The error bounds correspond to one standard deviation. Subtraction of the off-axis velocities from the on-axis velocity yields a velocity anomaly. Comparing the velocity-depth profiles for models 3, 4, and 5 shows that the velocities vary little on the ridge axis. Off axis, the three velocities vary little above a depth of 4.5 km bsf and differ by approximately 0.1 km/s. While for model 5 the estimated velocity anomaly is on the order of 0.4 km/s, the velocity anomaly is slightly larger for models 3 and 4. Furthermore, models 3 and 4 show off-axis velocities larger than 7.3 km/s inconsistent with pure gabbro in the lower crust [*Christensen*, 1979]. Therefore, model 5 is best suited for estimating crustal temperatures.

[44] To convert the velocity anomaly to a temperature anomaly, we apply relationships between temperature anomaly and velocity anomaly based on laboratory measurements for different gabbroic rocks [*Hughes and Maurette*, 1957; *Christensen*, 1979; *Bai et al.*, 2003]. We carried out a logarithmic linear regression for the velocity-temperature data for the MAR by *Christensen* [1979] for temperatures between 0°C and 300°C.

$$\log V = a \cdot T + V_0, \tag{2}$$

where V stands for the velocity as observed by *Christensen* [1979], T for the temperatures and V_0 for the velocity at room temperature. We excluded their data for temperatures above 300°C because of a detectable change in the T-V slope that is believed to have been caused by the opening of grain boundary pore spaces [*Christensen*, 1979]. We did the same for the data reported by *Bai et al.* [2003] for temperatures up to 700°C. We fit the data of *Hughes and Maurette* [1957] using a bilinear regression for both temperature and pressure. The logarithm of the velocity does not vary linearly with pressure [*Birch*, 1960, 1961; *Christensen*, 1984; *Wepfer and Christensen*, 1991a], but this approximation can remove part of the pressure effect. The different temperature-velocity gradients (Table 2) vary by an order of magnitude. *Dunn et al.* [2000] use the gradient given by *Christensen* [1979]; we test all three. For the anelastic case, we apply the relationship described by *Dunn et al.* [2000] and use an attenuation $Q \approx 100$ [*Wepfer and Christensen*, 1991b; *Wilcock et al.*, 1993]. The liquidus temperature was estimated using a relationship between the MgO number and the liquidus temperature T_l [*Sinton and Detrick*, 1992]:

$$T_l = 19.1 \cdot \mathrm{MgO} + 1054. \tag{3}$$

An MgO number between 6% and 10% [*Perfit and Chadwick*, 1998] gives liquidus temperatures of approximately 1170°C and 1245°C, respectively.

[45] We clip the calculated temperatures at the liquidus model for evolved Mg-poor mid-ocean ridge basalt compositions and explain the remaining velocity anomaly using partial melt. The resulting temperature distributions are shown in Figure 12b. The only velocity-temperature relationship that implies partial melt is based on the data set by *Bai et al.* [2003]. The amount of melt required to explain the remaining velocity anomaly is small: between 0.2% for thin films and 1.2% for spheres [*Schmeling*, 1985]. Doubling the velocity anomaly from 0.5 to 1.0 km/s requires a factor of 10 increase in melt fraction. Such an increase in velocity anomaly is possible (Appendix A). Comparing the effect of using velocity model 3 or 4 to estimate crustal temperatures shows the estimated temperatures change little above a depth of 4.5 km bsf. However, below this depth models 3 and 4 require higher crustal temperatures (Figure 12b).

[46] The uncertainties in estimating temperature and melt fractions are large. The calculation of the velocity anomaly, the selection of a temperature reference model, and the estimation of a temperature-velocity relation introduce errors into the calculation. In addition, the process of linking laboratory measurements of velocity and temperature is not straightforward, as length scales of laboratory measurements are very different from the length scales of seismic tomography experiments. Finally, it is not at all certain that lower crustal rocks are the same off axis as on axis. For example, if there is hydrothermal alteration of ultramafic off-axis rocks, they will tend to give a lower velocity for a given temperature [*Miller and Christensen*, 1997]. In this case, the temperature difference (and potentially the quantity of melt) required to explain the on-axis velocities would be greater. However, no ultramafic rocks have been observed off axis from the Lucky Strike segment center, but ultramafic rocks can be found at the Menez Hom massif forming the southern end of the Lucky Strike segment.

[47] That said, the measurements by *Christensen* [1979] on MAR gabbros suggest that the seismic velocity anomaly underneath the axial magma chamber of the Lucky Strike segment can be explained by the presence of increased temperatures only. Using velocity model 5 and the elastic relationship used by *Dunn et al.* [2000] a reasonable temperature estimate in the lower crustal region of decreased velocities is 800°C to 1000°C but the range of possible temperatures is larger. The presence of partial melt cannot be excluded, but is unlikely to be larger than 1%. The location of the greatest velocity anomaly, and therefore the most likely location of melt, is not directly beneath the

melt lens reflector but deeper in the crust. However, this could be an effect of smoothing of our velocity model.

7. Discussion

[48] For the following discussion, it is convenient to divide the crust in the Lucky Strike segment into upper crust (above 2 km bsf), middle crust (2–4 km bsf), and lower crust (below 3–4 km bsf). In the upper crust we observe a region of decreased velocities underneath the median valley, the middle crust is characterized by an along-axis velocity decrease toward the segment ends, and the lower crust shows a low-velocity anomaly underneath the axial melt lens reflector underneath the Lucky Strike volcano. Finally, we find a crustal thickness decrease toward the segment ends. Here, we discuss different processes explaining our observations.

7.1. Upper Crustal Low-Velocity Region in the Median Valley

[49] The upper crust shows a prominent region of decreased velocities, which runs parallel to the ridge axis and is limited by the median valley bounding faults (Figures 8 and 9). These decreased velocities are no longer observed at 2 km bsf (3–4 km bsl). The traveltime residuals vary azimuthally in this zone (Figure 11), consistent with the anisotropy which may be predicted due to the ridge parallel cracks. A similar upper crustal low-velocity region and ridge parallel anisotropy were observed on the OH-1 segment at 35°N [*Magde et al.*, 2000; *Dunn et al.*, 2005]. An important difference from the OH-1 segment is that the axial anisotropic zone occupies about the same extent as the upper crustal region of decreased velocities at Lucky Strike, whereas at OH-1 anisotropy is observed down to the upper mantle with a different fast direction in crust and mantle [*Dunn et al.*, 2005].

[50] Three mechanisms can control upper crustal porosities and thereby velocities: emplacement [*Herron*, 1982; *Harding et al.*, 1993], hydrothermal alteration and precipitation [*Houtz and Ewing*, 1976; *Grevemeyer and Weigel*, 1997], and active extension (faults, fractures, and fissures). Hydrothermal precipitation and the closure of pore spaces [*Carlson and Herrick*, 1990; *Wilkens et al.*, 1991; *Carlson*, 1998] can decrease the porosity causing a gradual velocity increase with crustal age and thereby distance from the ridge axis. At fast spreading ridges, upper crustal velocities depend on the presence of fresh lava and their alteration and the distribution of cracks [*Dunn and Toomey*, 2001], but faulting can play an important role at slow spreading ridges.

[51] We attribute the observed low velocities in the upper crust and the sinusoidal variation of traveltime residuals to increased porosities caused by ridge parallel fractures and fissures linked to ridge parallel faults, since this mechanism explains both observations. We do not consider hydrothermal alteration a possible explanation for the observed slow velocities because we do not observe any correlation of the low-velocity regions and hydrothermal circulation at the seafloor. However, the contrast between velocities on the ridge axis and velocities beneath the valley walls can be further increased by hydrothermal precipitation, which explains the gradual velocity increase outside the median valley. Finally, the low-velocity region inside the median valley could be linked to the presence of fresher, more porous lava. If segment end lava is fed from the magma chamber at the segment center, the basaltic crust at the segment ends would have to be produced by far-reaching dike injections. Dike injection events reaching tens of kilometers have been observed in Iceland [*Buck et al.*, 2006], Ethiopia [*Wright et al.*, 2006; *Doubre et al.*, 2007], and Axial Volcano on the Juan de Fuca Ridge [*Dziak and Fox*, 1999]. However, it cannot be ruled out that melt has ever entered the crust away from the segment center.

[52] Faulting should have the greatest effect in the upper crust because the population of faults, fractures, and fissures decreases with depth, and few faults penetrate to the base of the crust. This behavior is consistent with the ridge parallel seismic anisotropy we observe in the upper 3–4 km bsf. However, the seismic anisotropy seems to continue to greater depth than the low-velocity anomaly.

7.2. Lower Crustal Low-Velocity Region Underlying a Melt Lens Reflector

[53] Between a depth of 3.5 km bsf and the Moho a region of decreased velocities is observed with velocities ~0.5 km/s lower than in the surrounding rock (Figures 8 and 9). The lateral extent of the velocity anomaly appears narrower along axis than across axis. A similar lower crustal velocity anomaly in the segment center was observed for the OH-1 segment [*Magde et al.*, 2000; *Hooft et al.*, 2000; *Dunn et al.*, 2005], which they interpret as caused by elevated temperatures and possibly melt. *Navin et al.* [1998] also report a similar low-velocity anomaly for the ridge axis of the Reykjanes Ridge with velocities 0.5 km/s lower than off axis.

[54] The low velocities probably outline the pathway of melt to the melt lens, even though the velocities do not require any melt presently. The lateral asymmetry of the low-velocity anomaly could be caused by injection of hotter material underneath the segment center and subsequent across-axis rifting of hotter material. There are different explanations for why no melt is observed underneath the axial melt lens reflector.

[55] 1. No melt is detected due to limitations of traveltime tomography. There is a magma chamber beneath the melt lens, but the high-melt region is too small to be imaged by tomography due to wavefront healing. Indeed, the estimated velocity anomaly is the smallest deviation that can fit the data. The velocities we observed are smoothed, hence the velocity anomaly is smaller leading to poor constraints on the melt content. Lower velocities, requiring larger amounts of melt, are also consistent with the data, but not with the imposed smoothness constraint.

[56] 2. No melt is present due to the current state of the ridge segment. The melt supply may have ended and the melt lens and magma chamber are dying out, so there is still melt present in the axial melt lens, but the magma chamber underneath does not contain any melt. Alternatively, the region of decreased velocities corresponds to a current melt percolation zone with very little melt.

7.3. Midcrustal Velocity Decrease Toward the Segment Ends

[57] Between about 2 and 4 km bsf depth, a band of increased velocities runs approximately east to west across

the segment center (Figure 9). Velocities in this band are approximately 1.5 km/s faster than velocities at the same depth at the segment ends. *Hooft et al.* [2000] observe similar low velocities close to the Oceanographer fracture zone, which they interpret as the result of fracturing and alteration.

[58] At the segment ends, faults linked to the nontransform offsets limiting the ridge segment are observed orthogonal to the ridge axis, whereas faults at the segment center run mostly parallel to the ridge axis. This deformation is likely to increase the porosity of the rock, which would explain the observed velocity decrease between a depth of 2 and 4 km bsf. We propose that the segment ends are likely to be affected by large offset normal faulting leading to extensive fracturing and local exhumation and alteration of mantle material [*Cannat et al.*, 1995], which creates a lower velocity middle crust. While the segment center is magmatically dominated, tectonics are more important at the segment ends consistent observations south of the Oceanographer fracture zone [*Hooft et al.*, 2000].

[59] The high-velocity band in the segment center at a depth of 2–3 km bsf is not uniform, but contains isolated zones with even higher velocities (Figure 9). Possible explanations for these isolated zones are as follows: (1) The high-velocity regions are linked to preferred hydrothermal fluid pathways, as hydrothermal precipitation decreases porosity and increases crustal velocities. (2) The velocity structure of the material is altered by faulting after emplacement causing a local change in velocity. (3) The high velocities could be related to magmatically active periods and cooled intrusive bodies with larger grain size and fewer cracks, whereas the regions of reduced velocities correspond to periods dominated by tectonics. In scenarios 2 and 3, tectonic processes will alter the porosity structure of the crust decreasing the seismic velocities.

7.4. Crustal Thickness Variations

[60] The average crustal thickness of 7–8 km at the segment center of the Lucky Strike segment is similar to the crustal thickness beneath the Reykjanes Ridge [*Navin et al.*, 1998]. An average crustal thickness for the whole Lucky Strike segment is difficult to estimate since only the central 30 km of the ridge segment is constrained by our data. While the Moho at the segment ends is not constrained, our models indicate that the crust thins by at least 1.5 km from the segment center to the segment ends (Figure 6). In the OH-1 segment, the thicker crust at the segment center is interpreted as enhanced melt delivery to the segment center [*Hooft et al.*, 2000; *Dunn et al.*, 2005]. The thickened crust in the segment center of the Lucky Strike segment can be explained in a similar fashion, although the crustal thickness variations are larger in the OH-1 segment. An additional mechanism possibly causing a thinning of the crust at the segment ends is tectonic stretching. The along-axis variations in crustal thickness agree well with predictions based on prior gravity measurements [*Detrick et al.*, 1995; *Escartín et al.*, 2001].

[61] Finally, the crust is thickest off axis to the west of the volcano (Figure 6). The crustal thickness maximum correlates with the existence of a rifted previous volcano off axis, which has been faulted asymmetrically into the new ridge flank [*Escartin et al.*, 2005]. If the observed region of decreased velocities in the lower crust is indeed linked to the melt percolation system, the magmatic source in the mantle would be underlying the axial melt lens and lower crustal low-velocity region. In that case, an explanation for the westward thickening of the crust could be a recent shift of the magmatic source to the east. In this scenario the thicker crust in the west would correspond to an old accretion center, whereas the region of decreased velocities in the lower crust and axial melt lens reflection mark today's accretion center. We do not consider a magmatic source in the mantle that is offset away from the ridge axis as observed on the East Pacific Rise [*Crawford and Webb*, 2002; *Toomey et al.*, 2007] a viable explanation for our observation due to the spatial separation between the crustal thickness maximum and the lower crustal low-velocity region.

7.5. Implications for Magmatic, Tectonic, and Hydrothermal Processes

[62] Integrating our different observations in the Lucky Strike segment allows us to characterize the role of different processes active in crustal accretion. While hydrothermal processes are variable in time [*Lalou et al.*, 1995], our observations indicate that hydrothermal circulation has been active over ~2 Ma constrained by our model. While magmatic accretion at the segment center is episodic, tectonic processes are occurring more continuously.

[63] For the lower crust below the axial melt lens reflector we speculate that magmatic processes dominate crustal accretion at least at the current time, since no evidence for deep faulting has been observed. The observed along-axis crustal thickness maximum is a clear indication that melt flux is focused at the segment center [*Schouten et al.*, 1985; *Tolstoy et al.*, 1993] either by diapiric mantle upwelling or by focusing of melt in the upper mantle [*Hooft et al.*, 2000]. This melt flux to the segment center has created the axial melt lens and the Lucky Strike volcano; the underlying zone of anomalously low velocities marks the pathway of melt into the axial melt lens. The magmatic input into the Lucky Strike segment is not stable over time. The off-axis crustal thickness maximum and rifted volcano are likely linked to a prior accretion center that has been rifted off axis and integrated into the median valley wall. While the lower crust at the segment center is characterized by magmatic processes, tectonic processes linked to large offset normal faults and local exhumation combined with alteration of mantle material are important at the segment ends [*Cannat et al.*, 1995]. These processes are responsible for the low velocity lower crust and the reduced crustal thickness at the segment ends.

[64] At shallow depths, above the depth of the axial melt lens reflector, we find evidence for the current activity of hydrothermal, tectonic, and magmatic processes. A large amount of the melt that had been fed into the axial magma chamber has erupted [*Fouquet et al.*, 1995] contributing to the construction of the Lucky Strike volcano. A smaller amount of melt has probably been redistributed along the ridge axis creating smaller volcanic edifices observed along the seafloor [*Ondréas et al.*, 1997; *Gracia et al.*, 1998]. These recent magmatic events like the recent dyke injection event [*Dziak et al.*, 2004] may be responsible for some of the lowest velocities observed in the near surface. However,

Table A1. Checkerboard Patterns[a]

Pattern	Δ_x, Δ_y (km)	Δ_z (km)	λ_x, λ_y (km)	λ_z (km)
I	1.95	0.39	7.89	1.58
II	1.95	0.39	11.68	2.37
III	1.95	0.39	15.58	3.15
IV	1.95	0.39	23.37	4.73
V	0.5	–	10	–
VI	0.5	–	20	–

[a]Δ_x, Δ_y and Δ_z give the approximate node spacing of the velocity/interface model. λ_x, λ_y, and λ_z denote the wavelength of the checkerboard pattern added to the best fitting/interface velocity model. Patterns I to IV were used for checkerboard testing of the velocity model. Patterns V and VI were used for checkerboard testing of the interface model.

extensional (faults, fractures, and fissures) are observed to be active throughout the median valley and are currently rifting the Lucky Strike volcano [*Humphris et al.*, 2002; *Escartín et al.*, 2008]. In our opinion these processes are the source for the observed upper crustal velocity anisotropy and the low-velocity region parallel to the ridge axis. Finally, while hydrothermal discharge has only been reported at the segment center [*Langmuir et al.*, 1997], hydrothermal circulation may not be limited Lucky Strike volcano. Off-axis hydrothermal circulation is our preferred explanation for the velocity increase with crustal age [*Jacobson*, 1992; *Shaw*, 1994; *Grevemeyer et al.*, 1998].

8. Conclusions

[65] The Lucky Strike seismic refraction experiment has yielded new insights into the crustal velocity structure in the Lucky Strike segment of the slow spreading MAR. The 3-D crustal velocity structure appears to be very similar to the one observed at the OH-1 segment at 35°N [*Magde et al.*, 1997; *Barclay et al.*, 1998; *Dunn et al.*, 2005].

[66] The upper crust is characterized by low velocities and a steep velocity gradient, while the lower crust shows high velocities and a flat velocity gradient. For our best fitting velocity model we observe a region of decreased velocities in the upper crust coincident with the median valley and a sinusoidal variation of traveltime residuals with azimuth. We interpret these observations as evidence for ridge parallel cracks linked to ridge parallel faulting. The velocity contrast across the median valley bounding faults is further enhanced by the aging of the crust.

[67] We image a region of decreased velocities starting at a depth of approximately 5 km bsl (3.5 km bsf). This region underlies an axial melt lens reflector at a depth of approximately 3 to 3.5 km bsf. Using a conservative estimate the low-velocity zone can be explained by elevated temperatures (800°C to 1000°C) and possibly small amounts of remnant melt (less than 1%). We associate the limits of the low-velocity region with the outer limits of the axial magma chamber and the magma feeding system of the axial melt lens.

[68] Crustal velocities decrease toward the segment ends. This velocity decrease is probably linked to a porosity increase due to the presence of faults at the segment ends or the alteration of exhumed mantle rocks.

[69] Finally, the crust thins toward the segment ends. We link this crustal thinning to focusing of melt at the segment center and tectonic thinning of the crust toward the segment ends. The thickest crust can be observed in the west of the Lucky Strike volcano, which can be explained by recent shift of the magmatic pulse to the segment center.

Appendix A: Resolution of the Velocity and Interface Models

[70] We applied checkerboard tests to systematically test the resolvability of anomalies with certain wavelength characteristics. Because of the different horizontal and vertical discretization and resolution, we chose checkerboards with one horizontal wavelength $\lambda_x = \lambda_y$ and a different vertical wavelength λ_z. We tested four different wavelength patterns (Table A1). The wavelength (i.e., the distance between two maxima) of the patterns increases from pattern I to pattern IV. The wavelength of pattern I (7.89 km horizontally, 1.58 km vertically) corresponds to approximately four times the node spacing, whereas the wavelength of pattern IV (23.37 km horizontally, 4.73 km vertically) corresponds to 12 grid nodes.

[71] Comparing the velocity model used in the forward calculation and the one recovered by the inversion shows where anomalies can be successfully reconstructed (Figure A1). For the interpretation of resolvability *Zelt* [1998] suggests that a resolvability below 0.7 marks unconstrained velocity nodes.

[72] Overall, the resolvability is highest between 3 and 6 km bsl (1.5 to 4.5 km bsf) (Figure A2). This is also the region with the largest ray density. Above 3 km bsl (~1.5 km bsf) the resolvability decreases for all four anomaly patterns, although the ray density is very high. This is caused by the geometry of the raypaths; there are plenty of rays near the surface, but few of them cross. Beneath 6 km bsl (~4.5 km bsf), the resolvability of short- and medium-wavelength anomalies (patterns I, II, and III) drops abruptly. Short-wavelength anomalies (pattern I) are not recovered at all for depths larger than 7 km bsl (5.5 km bsf). Medium-wavelength anomalies (patterns II and III) are resolved throughout the lower crust, except at the model edges, but the resolvability decreases with depth because of the smaller number of passing rays. Large-scale anomalies (pattern IV) are recovered throughout the model.

[73] When inverting for the depth of a reflecting interface such as the Moho, the quality of the interface model should be examined carefully. This is especially important in the absence of any ray phases penetrating below the interface. Plotting the PmP reflection points demonstrates where the interface position is constrained by observations. These reflection points are a 2-D equivalent to the 3-D ray density used for the velocity model. Checkerboard tests can serve as an additional measure of testing the resolution of the interface model. The procedure is analogous to that used for the velocity model. A perturbation is added to the best fitting interface model. The maximum depth perturbation we applied to construct the tested checkerboard is 500 m. We then estimated synthetic traveltimes, added noise, and used the data as input for an inversion. The perturbation applied to the best fitting interface model is of the same magnitude as the difference observed between interface

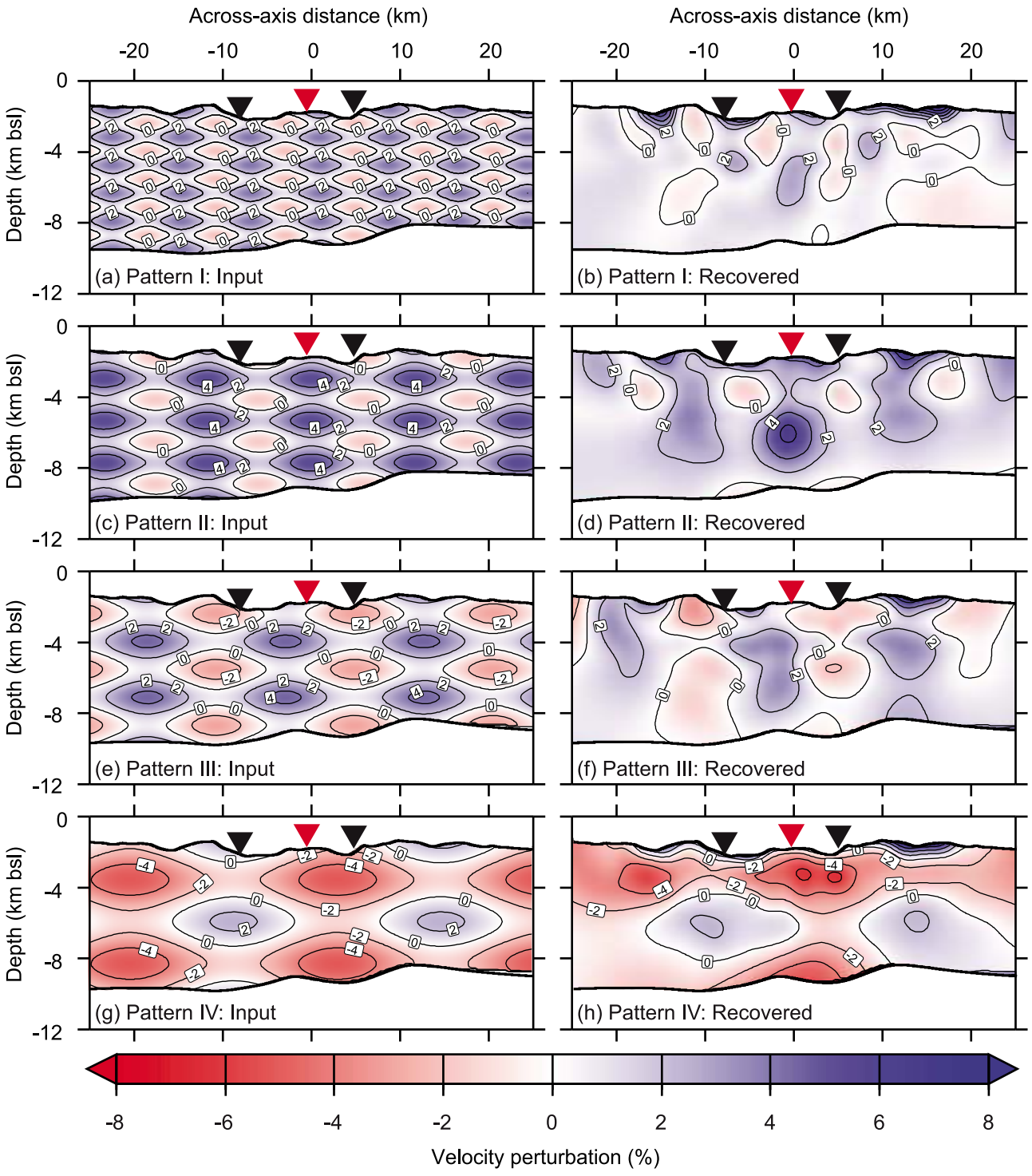

Figure A1. Examples of the checkerboard patterns used in the estimation of the resolvability. The perturbations applied to the best fitting velocity model are given for patterns (a) I, (c) II, (e) III, and (g) IV (Table A1). The recovered anomalies are given for patterns (b) I, (d) II, (f) III, and (h) IV. The vertical exaggeration is 2:1. The vertical slices run orthogonal to the ridge axis at an along-axis distance of 0 km (Figure 1). The red triangle marks the position of the Lucky Strike volcano, and the black triangles mark the eastern and western bounding faults.

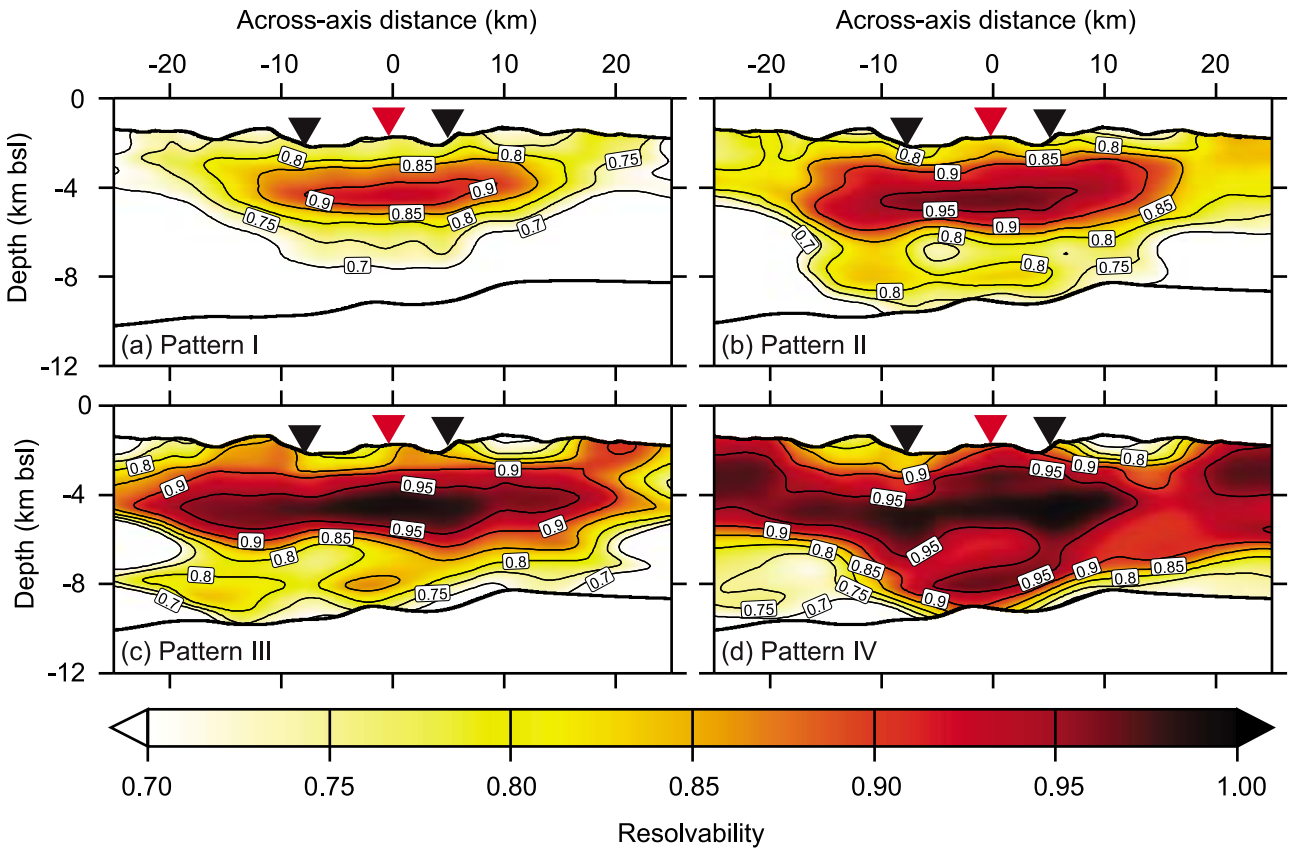

Figure A2. Resolvability for the four different checkerboard patterns shown in Figure A1. The vertical slices run orthogonal to the ridge axis at an along-axis distance of 0 km. The resolvability or averaged semblance is given for checkerboard patterns (a) I, (b) II, (c) III, and (d) IV (Table A1). The vertical exaggeration is 2:1.

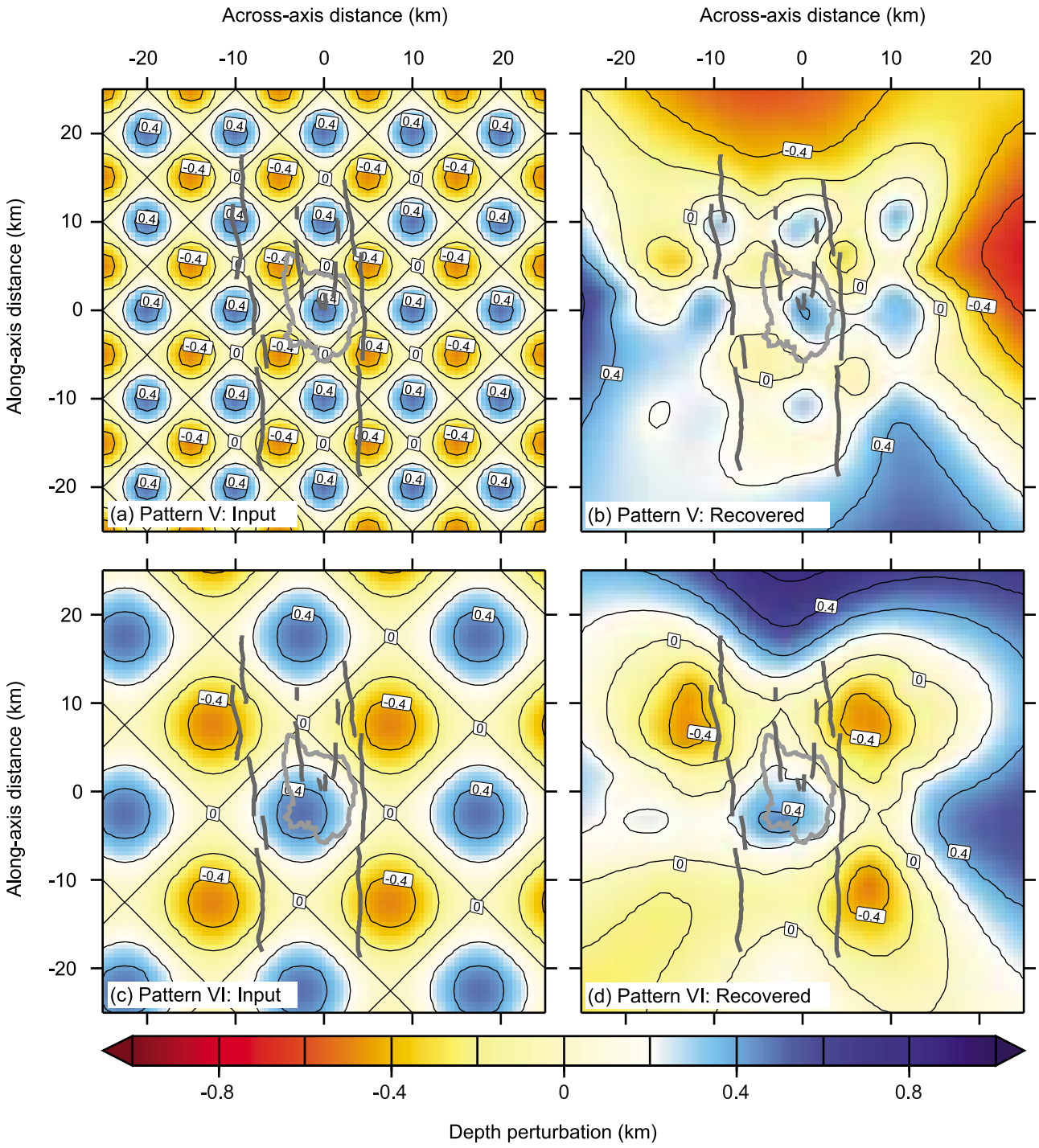

Figure A3. Checkerboard tests for interface variations with two different wavelength. (a) The perturbations for pattern V (Table A1) used in the forward calculation. (b) The perturbations recovered by the inversion. (c) The perturbations for pattern VI (Table A1). (d) The perturbations recovered by the inversion. The area corresponds to the 50 km × 50 km area shown in Figure 1. The light gray line marks the position of the volcano's 2 km depth contour, and the dark gray lines mark the position of major faults.

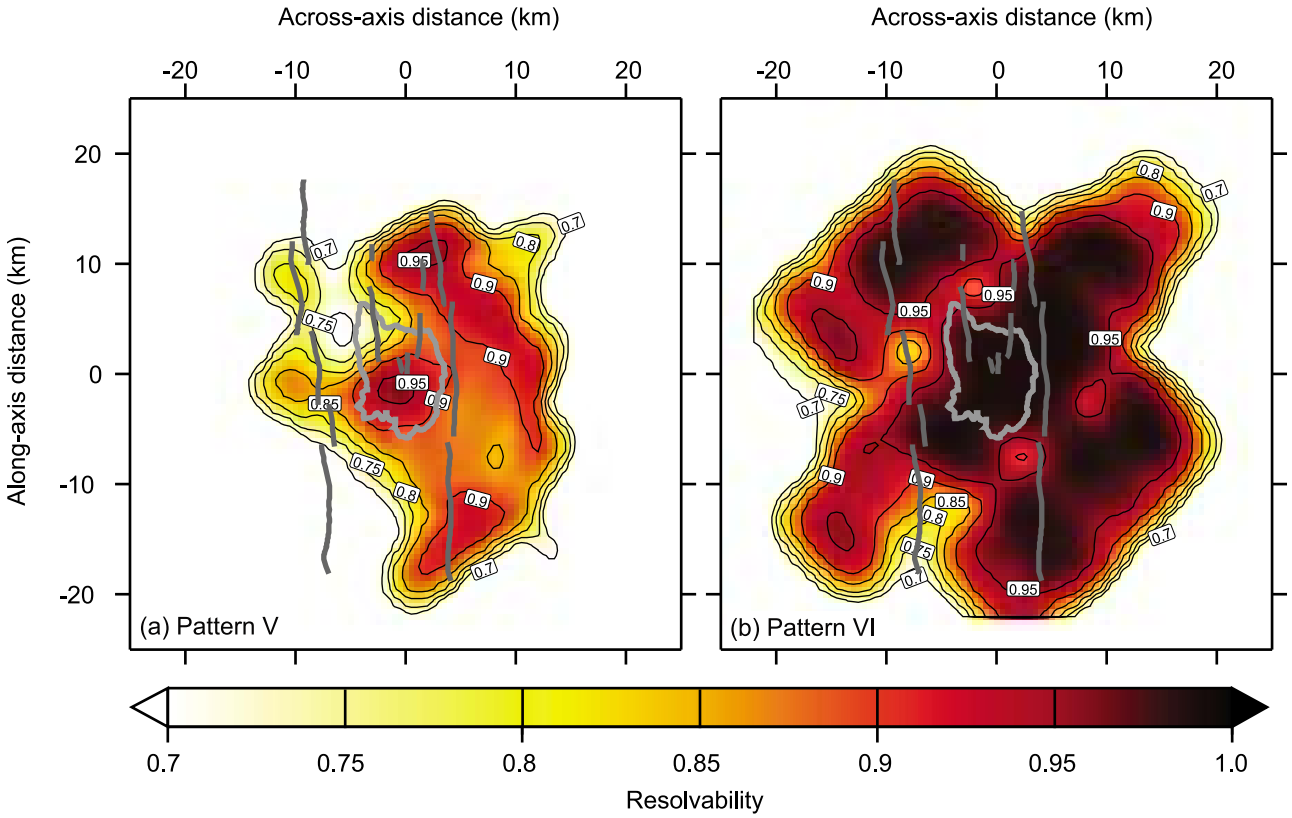

Figure A4. Resolvability or averaged semblance using checkerboard patterns (a) V and (b) VI for interface variations. The resolvability included the checkerboards shown in Figure A3. The area corresponds to the 50 km × 50 km area shown in Figure 1. The light gray line marks the position of the volcano's 2 km depth contour, and the dark gray lines mark the position of major faults.

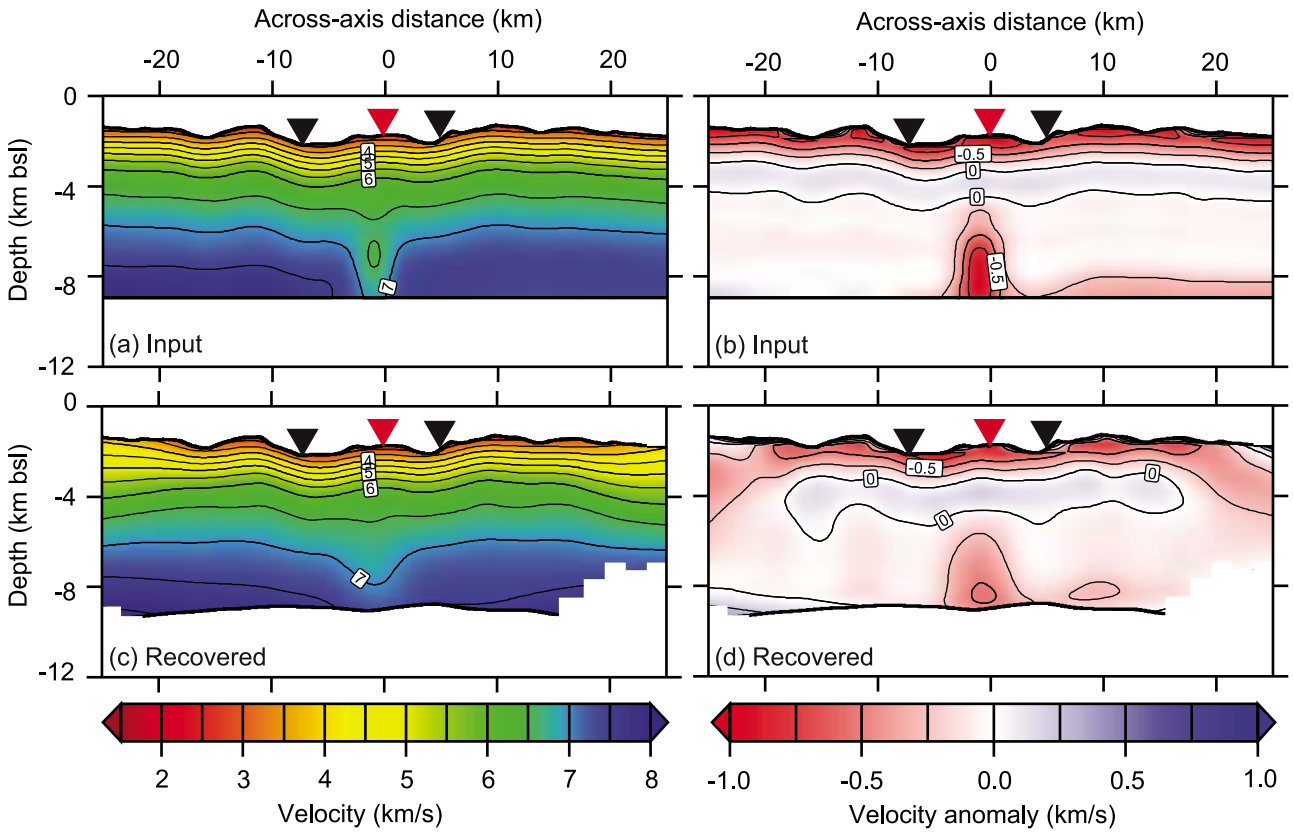

Figure A5. Sharp anomaly recovery test for a lower crustal low-velocity zone. (a and b) The seismic velocity or seismic anomaly used in the modeling of the synthetic data. (c and d) The seismic velocity and seismic anomaly recovered by the inversion. For comparability the seismic velocity anomalies were calculated by subtracting the same reference velocity model from both velocity distributions. The distribution of shots and receivers was the same as used in the experiment described in this article. The black triangles mark the location of the eastern and western bounding faults at the surface. The red triangle indicates the position of the Lucky Strike volcano. Again, the slices shown here run across the ridge axis at an along-axis distance of 0 km.

models 3, 4, and 5 (Figure 6). For a fixed set of inversion parameters we can recover perturbations that are smaller than variations between equivalent models derived by changing the inversion parameters. Here, we tested checkerboard patterns with two spatial wavelengths, one 10 km and the other 20 km (Table A1).

[74] Checkerboard tests show that the interface model is well constrained below the Lucky Strike volcano (Figure A3). The interface parameters are recovered by the inversion between −15 km and 15 km across axis and between −15 km and 15 km along axis, except for the southwestern part of the model (Figure A3), where very few reflected phases were recorded (Figure A4).

[75] One of the most interesting features of our velocity models is the lower crustal low-velocity anomaly underlying the axial melt lens reflector [*Singh et al.*, 2006; *Combier*, 2007]. Generally, the velocity inside low-velocity regions is difficult to constrain, because seismic waves rarely penetrate the low-velocity body. To test the constraint on the amplitude of the low-velocity region, we created a synthetic low-velocity region underneath the axial melt lens reflector coincident with the position of the observed low-velocity region. The velocity inside the low-velocity region was approximately 1 km/s slower than in the surrounding medium. Next, we estimated synthetic traveltimes using the same distribution of traveltime observations as during the field experiment and added Gaussian noise corresponding to the observed traveltime uncertainties (31 ms Pg and 34 ms PmP). Those data were used as input for our inversion. The input and recovered velocity model are shown in Figure A5. While the location of the anomaly is approximately reconstructed, the amplitude of the low-velocity region recovered is much weaker than the input value. This implies that the velocities in the low-velocity region underneath the axial melt lens reflector could be significantly lower than inside our velocity model.

[76] **Acknowledgments.** This work was made possible by the EU Marie Curie RTN Momarnet, Institut de Physique du Globe de Paris, CNRS/INSU, Ifremer, and the country of Portugal. The OBS operations were assured by Laurent Béguery, Oualid Aouji, Carlos Corela, and Jose Duarte. Crew and captain of the French research vessel N/O L'Atalante helped us to make this project a success. Moreover, this manuscript profited greatly from the suggestions made by two anonymous reviewers and from discussions with Juan-Pablo Canales, Javier Escartín, William Wilcock, and Ingo Grevemeyer.

References

Avedik, F., V. Renard, J. Allenou, and B. Morvan (1993), "Single bubble" air-gun array for deep exploration, *Geophysics*, *58*(3), 366–382, doi:10.1190/1.1443420.

Avedik, F., V. Hirn, A. Renard, R. Nicolich, J. Olivet, and M. Sachapazi (1996), "Single-bubble" marine source offers new perspectives for lithospheric exploration, *Tectonophysics*, *267*, 57–71, doi:10.1016/S0040-1951(96)00112-6.

Backus, G. (1965), Possible forms of seismic anisotropy of the uppermost mantle under oceans, *J. Geophys. Res.*, *70*(14), 3429–3439, doi:10.1029/JZ070i014p03429.

Bai, L., J. Du, W. Liu, and W. Zhou (2003), Experimental studies of electrical conductivities and p-wave velocities of gabbro at high pressures and high temperatures, *Sci. China D*, *46*(9), 895–908, doi:10.1360/01yd0441.

Banerjee, B., and S. Das Gupta (1977), Gravitational attraction of a rectangular parallelepiped, *Geophysics*, *42*(5), 1053–1055, doi:10.1190/1.1440766.

Barclay, A., D. Toomey, and S. Solomon (1998), Seismic structure and crustal magmatism at the Mid-Atlantic Ridge, 35°N, *J. Geophys. Res.*, *103*(B8), 17,827–17,844, doi:10.1029/98JB01275.

Barker, N. (2004), Electromagnetic investigation of the Lucky Strike seamount near 37°N, Mid-Atlantic Ridge, Ph.D. thesis, Univ. of Southampton, Southampton, U. K.

Bazin, S., et al. (2001), Three-dimensional shallow crustal emplacement at the 9°03′N overlapping spreading center on the East Pacific Rise: Correlations between magnetization and tomographic images, *J. Geophys. Res.*, *106*(B8), 16,101–16,117, doi:10.1029/2001JB000371.

Birch, F. (1960), The velocity of compressional waves in rocks to 10 kilobars: Part 1, *J. Geophys. Res.*, *65*(4), 1083–1100, doi:10.1029/JZ065i004p01083.

Birch, F. (1961), The velocity of compressional waves in rocks to 10 kilobars: Part 2, *J. Geophys. Res.*, *66*(7), 2199–2224, doi:10.1029/JZ066i007p02199.

Blacic, T., G. Ito, J. Canales, R. Detrick, and J. Sinton (2004), Constructing the crust along the Galapagos spreading center 91.3°–95.5°W: Correlation of seismic layer 2A with axial magma lens and topographic characteristics, *J. Geophys. Res.*, *109*, B10310, doi:10.1029/2004JB003066.

Buck, W., P. Einarsson, and B. Brandsóttir (2006), Tectonic stress and magma chamber size as controls on dike propagation: Constraints from the 1975–1984 Krafla rifting episode, *J. Geophys. Res.*, *111*, B12404, doi:10.1029/2005JB003879.

Buttkus, B. (2000), *Spectral Analysis and Filter Theory in Applied Geophysics*, 1st ed., Springer, Berlin.

Calvert, A. J. (1995), Seismic evidence for a magma chamber beneath the slow spreading Mid-Atlantic Ridge, *Nature*, *377*, 410–414, doi:10.1038/377410a0.

Calvert, A. J. (1997), Backscattered coherent noise and seismic reflection imaging of the oceanic crust: An example from the rift valley of the Mid-Atlantic Ridge at 23°N, *J. Geophys. Res.*, *102*(B3), 5119–5133, doi:10.1029/96JB03798.

Canales, J., J. Collins, J. Escartin, and R. Detrick (2000), Seismic structure across the rift valley of the Mid-Atlantic Ridge at 23°20′ (MARK area): Implications for crustal accretion processes at slow spreading ridges, *J. Geophys. Res.*, *105*(B12), 28,411–28,425, doi:10.1029/2000JB900301.

Cannat, M., et al. (1995), Thin crust, ultramafic exposures and rugged faulting patterns at the Mid-Atlantic Ridge (22°–24°N), *Geology*, *23*(1), 49–52, doi:10.1130/0091-7613(1995)023<0049:TCUEAR>2.3.CO;2.

Cannat, M., et al. (1999), Mid-Atlantic Ridge-Azores hotspot interactions: Along-axis migration of a hotspot-derived event of enhanced magmatism 10 to 4 Ma ago, *Earth Planet. Sci. Lett.*, *173*, 257–269, doi:10.1016/S0012-821X(99)00234-4.

Carlson, R. (1998), Seismic velocities in the uppermost oceanic crust: Age dependence and the fate of layer 2A, *J. Geophys. Res.*, *103*(B4), 7069–7077, doi:10.1029/97JB03577.

Carlson, R., and C. Herrick (1990), Densities and porosities in the oceanic crust and their variations with depth and age, *J. Geophys. Res.*, *95*(B6), 9153–9170, doi:10.1029/JB095iB06p09153.

Carlson, R., and G. Raskin (1984), Density of the ocean crust, *Nature*, *311*, 555–558, doi:10.1038/311555a0.

Chen, Y., and W. Morgan (1990), A nonlinear rheology model for mid-ocean ridge axis topography, *J. Geophys. Res.*, *95*(B11), 17,583–17,604, doi:10.1029/JB095iB11p17583.

Christensen, N. (1979), Compressional wave velocities in rocks at high temperatures and pressures, critical thermal gradients and crustal low-velocity zones, *J. Geophys. Res.*, *84*(B12), 6849–6857, doi:10.1029/JB084iB12p06849.

Christensen, N. (1984), Pore pressure and oceanic crustal seismic structure, *Geophys. J. R. Astron. Soc.*, *79*, 411–423.

Cochran, J., and M. Talwani (1978), Gravity anomalies, regional elevation, and the deep structure of the North Atlantic, *J. Geophys. Res.*, *83*(B10), 4907–4924, doi:10.1029/JB083iB10p04907.

Combier, V. (2007), Mid-ocean ridge processes: Insights from 3D reflection seismics at the 9°N OSC on the East Pacific Rise, and the Lucky Strike Volcano on the Mid-Atlantic Ridge, Ph.D. thesis, Inst. de Phys. du Globe de Paris, Paris.

Constable, S., R. Parker, and C. Constable (1987), Occam's inversion: A practical algorithm for generating smooth models from electromagnetic data, *Geophysics*, *52*(3), 289–300, doi:10.1190/1.1442303.

Corliss, J., et al. (1979), Submarine thermal springs on the Galápagos rift, *Science*, *203*(4385), 1073–1082, doi:10.1126/science.203.4385.1073.

Crawford, W., and S. Webb (2002), Variations in the distribution of magma in the lower crust and at the Moho beneath the East Pacific Rise at 9°–10°N, *Earth Planet. Sci. Lett.*, *203*, 117–130, doi:10.1016/S0012-821X(02)00831-2.

Creager, K., and L. Dorman (1982), Location of instruments on the seafloor by joint adjustment of instrument and ship positions, *J. Geophys. Res.*, *87*(B10), 8379–8388, doi:10.1029/JB087iB10p08379.

deGroot Hedlin, C., and S. Constable (1990), Occam's inversion to generate smooth, two-dimensional models from magnetotelluric data, *Geophysics*, *55*(12), 1613–1624, doi:10.1190/1.1442813.

Detrick, R., P. Buhl, E. Vera, J. Mutter, J. Orcutt, J. Madsen, and T. Brocher (1987), Multi-channel seismic imaging of a crustal magma chamber along the East Pacific Rise, *Nature*, *326*, 35–41, doi:10.1038/326035a0.

Detrick, R., J. Mutter, P. Buhl, and I. Kim (1990), No evidence from multichannel reflection data for a crustal magma chamber in the MARK area on the Mid-Atlantic Ridge, *Nature*, *347*, 61–64, doi:10.1038/347061a0.

Detrick, R., H. Needham, and V. Renard (1995), Gravity anomalies and crustal thickness variations along the Mid-atlantic Ridge between 33°N and 40°N, *J. Geophys. Res.*, *100*(B3), 3767–3787, doi:10.1029/94JB02649.

Doubre, C., I. Manighetti, C. Dorbath, L. Dorbath, E. Jacques, and J. Delmond (2007), Crustal structure and magmato-tectonic processes in an active rift (Asal-Ghobbet, Afar, East Africa): 1. Insights from a 5-month seismological experiment, *J. Geophys. Res.*, *112*, B05405, doi:10.1029/2005JB003940.

Dunn, R., and D. Toomey (1997), Seismological evidence for three-dimensional melt migration beneath the East Pacific Rise, *Nature*, *388*, 259–262, doi:10.1038/40831.

Dunn, R., and D. Toomey (2001), Crack-induced seismic anisotropy in the oceanic crust across the East Pacific Rise (9°30′N), *Earth Planet. Sci. Lett.*, *189*, 9–17, doi:10.1016/S0012-821X(01)00353-3.

Dunn, R., D. Toomey, and S. Solomon (2000), Three-dimensional seismic structure and physical properties of the crust and shallow mantle beneath the East Pacific Rise at 9°30′N, *J. Geophys. Res.*, *105*(B10), 23,537–23,555, doi:10.1029/2000JB900210.

Dunn, R. A., V. Lekic, R. S. Detrick, and D. R. Toomey (2005), Three-dimensional seismic structure of the Mid-Atlantic Ridge (35°N): Evidence for focused melt supply and lower crustal dike injection, *J. Geophys. Res.*, *110*, B09101, doi:10.1029/2004JB003473.

Dusunur, D. (2008), Thermal structure of mid-ocean ridges (Lucky Strike, Mid-Atlantic Ridge) and magma chambers, Ph.D. thesis, Inst. de Phys. du Globe de Paris, Paris.

Dusunur, D., J. Escartin, V. Combier, T. Seher, W. Crawford, M. Cannat, S. Singh, L. Matias, and J. Miranda (2009), Seismological constraints on the thermal structure along the Lucky Strike segment (Mid-Atlantic Ridge) and interaction of tectonic and magmatic processes around the magma chambers, *Mar. Geophys. Res.*, *30*(2), 105–120, doi:10.1007/s11001-009-9071-3.

Dziak, R., and C. Fox (1999), The January 1998 earthquake swarm at Axial Volcano, Juan de Fuca Ridge: Hydroacoustic evidence of seafloor volcanic activity, *Geophys. Res. Lett.*, *26*(23), 3429–3432, doi:10.1029/1999GL002332.

Dziak, R., D. Smith, D. Bohnenstiehl, C. Fox, D. Desbruyeres, H. Matsumoto, M. Tolsoty, and D. Fornari (2004), Evidence of a recent magma dike intrusion at the slow spreading Lucky Strike segment, Mid-Atlantic Ridges, *J. Geophys. Res.*, *109*, B12102, doi:10.1029/2004JB003141.

Escartín, J., M. Cannat, G. Pouliquen, and A. Rabain (2001), Crustal thickness of V-shaped ridges south of the Azores: Interaction of the Mid-Atlantic Ridge (36°N–39°N) and the Azores hot spot, *J. Geophys. Res.*, *106*(B10), 21,719–21,735, doi:10.1029/2001JB000224.

Escartín, J., J. S. Soule, D. Fornari, M. Cannat, and S. Humphris (2005), Tectonic and volcanic interaction along the Lucky Strike rift valley floor: Constraints on hydrothermal distribution, *Eos Trans. AGU*, *86*(52), Fall Meet. Suppl., Abstract OS33A-1463.

Escartín, J., R. García, O. Delaunoy, J. Ferrer, N. Gracias, A. Elibol, X. Cufi, L. N. D. Fornari, S. Humphris, and J. Renard (2008), Globally aligned photomosaic of the Lucky Strike hydrothermal vent field (Mid-Atlantic Ridge, 37°50′N): Release of georeferenced data, mosaic construction, and viewing software, *Geochem. Geophys. Geosyst.*, *9*, Q12009, doi:10.1029/2008GC002204.

Fouquet, Y., J.-L. Charlou, I. Costa, J.-P. Donval, J. Radford-Knoery, H. Pellé, H. Ondréas, N. Lourenço, M. Ségonzac, and M. Kingston Tivey (1994), A detailed study of the Lucky Strike hydrothermal site and discovery of a new hydrothermal site: Menez Gwen: Preliminary results of the DIVA1 cruise (5–29 May, 1994), *InterRidge News*, *3*(2), 14–17.

Fouquet, Y., H. Ondréas, J.-L. Charlou, J.-P. Donval, J. Radford-Knoery, I. Costa, N. Lourenço, and M. Tivey (1995), Atlantic lava lakes and hot vents, *Nature*, *377*, 201, doi:10.1038/377201a0.

Fouquet, Y., J.-L. Charlou, and F. Barriga (2002), Modern seafloor hydrothermal deposits hosted in ultramafic rocks, *Geol. Soc. of Am. Abstr. Programs*, *34*, 194–197.

Gracia, E., L. Parson, and D. Bideau (1998), Volcano-tectonic variability along segments of the Mid-Atlantic Ridge between Azores platform and Hayes fracture zone: Evidence from submersible and high-resolution sidescan sonar data, in *Modern Ocean Floor Processes and the Geological Record*, edited by R. Mills and K. Harrison, *Geol. Soc. Spec. Publ.*, *148*, 1–15, doi:10.1144/GSL.SP.1998.148.01.01.

Grevemeyer, I., and W. Weigel (1997), Increase of seismic velocities in upper oceanic crust: The "superfast" spreading East Pacific Rise, *Geophys. Res. Lett.*, *24*(3), 217–220, doi:10.1029/96GL04005.

Grevemeyer, I., W. Weigel, and C. Jennrich (1998), Structure and ageing of oceanic crust at 14°S on the East Pacific Rise, *Geophys. J. Int.*, *135*, 573–584, doi:10.1046/j.1365-246X.1998.00673.x.

Harding, A. J., G. M. Kent, and J. A. Orcutt (1993), A multichannel seismic investigation of upper crustal structure at 9°N on the East Pacific Rise: Implications for crustal accretion, *J. Geophys. Res.*, *98*(B8), 13,925–13,944, doi:10.1029/93JB00886.

Henstock, T., A. Woods, and R. White (1993), The accretion of oceanic crust by episodic sill intrusion, *J. Geophys. Res.*, *98*(B3), 4143–4161, doi:10.1029/92JB02661.

Herron, T. (1982), Lava flow layer-East Pacific Rise, *Geophys. Res. Lett.*, *9*(1), 17–20, doi:10.1029/GL009i001p00017.

Hobro, J. (1999), Three-dimensional tomographic inversion of combined reflection and refraction seismic travel time data, Ph.D. thesis, Univ. of Cambridge, Cambridge, U. K.

Hobro, J., S. Singh, and T. Minshull (2003), Three-dimensional tomographic inversion of combined reflection and refraction seismic traveltime data, *Geophys. J. Int.*, *152*, 79–93, doi:10.1046/j.1365-246X.2003.01822.x.

Hooft, E., R. Detrick, D. Toomey, J. Collins, and J. Lin (2000), Crustal thickness and structure along three contrasting spreading segments of the Mid-Atlantic Ridge, 33.5°–35°N, *J. Geophys. Res.*, *105*(B4), 8205–8226, doi:10.1029/1999JB900442.

Houtz, R., and E. Ewing (1976), Upper crustal structure as a function of plate age, *J. Geophys. Res.*, *81*(14), 2490–2498, doi:10.1029/JB081i014p02490.

Hughes, D., and C. Maurette (1957), Variation of elastic wave velocities in basic igneous rocks with pressure and temperature, *Geophysics*, *22*(1), 23–31, doi:10.1190/1.1438332.

Humphris, S. E., D. J. Fornari, D. S. Scheirer, C. R. German, and L. M. Parson (2002), Geotectonic setting of hydrothermal activity on the summit of Lucky Strike Seamount (37°17?N, Mid-Atlantic Ridge), *Geochem. Geophys. Geosyst.*, *3*(8), 1049, doi:10.1029/2001GC000284.

Hussenoeder, S. A., G. M. Kent, and R. S. Detrick (2002), Upper crustal seismic structure of the slow spreading Mid-Atlantic Ridge, 35°N: Constraints on volcanic emplacement processes, *J. Geophys. Res.*, *107*(B8), 2156, doi:10.1029/2001JB001691.

Ito, G. (2001), Reykjanes 'V'-shaped ridges originating from a pulsing and dehydrating mantle plume, *Nature*, *411*, 681–684, doi:10.1038/35079561.

Jacobson, R. (1992), Impact of crustal evolution on changes of the seismic properties of the uppermost ocean crust, *Rev. Geophys.*, *30*(1), 23–42, doi:10.1029/91RG02811.

Jean-Baptiste, P., H. A. V. A. Bougault, J.-L. Charlou, J. Radford-Knoery, Y. Fouquet, D. Needham, and C. German (1998), Mantle ^{3}He in hydrothermal vents and plume of the Lucky Strike site (MAR 37°17′N) and associated geothermal heat flux, *Earth Planet. Sci. Lett.*, *157*, 69–77, doi:10.1016/S0012-821X(98)00022-3.

Jousselin, D., and A. Nicolas (2000), The Moho transition zone in the Oman ophiolite-relation with wehrlites in the crust and dunites in the mantle, *Mar. Geophys. Res.*, *21*(3/4), 229–241, doi:10.1023/A:1026733019682.

Karson, J., and J. Brown (1988), Geologic setting of the Snake Pit hydrothermal site: An active vent field on the Mid-Atlantic Ridge, *Mar. Geophys. Res.*, *10*, 91–107, doi:10.1007/BF02424662.

Keeton, J. A., R. C. Searle, C. Peirce, B. Parsons, R. S. White, M. C. Sinha, B. J. Murton, and L. M. Parson (1997), Bathymetry of the Reykjanes ridge, *Mar. Geophys. Res.*, *19*(1), 55–64, doi:10.1023/A:1004266721393.

Kissling, E. (1988), Geotomography with local earthquake data, *Rev. Geophys.*, *26*(4), 659–698, doi:10.1029/RG026i004p00659.

Kusznir, N. J., and M. H. P. Bott (1976), A thermal study of the formation of oceanic crust, *Geophys. J. R. Astron. Soc.*, *47*(1), 83–95, doi:10.1111/j.1365-246X.1976.tb01264.x.

Lalou, C., G. Thompson, M. Arnold, E. Brichet, E. Druffel, and P. Rona (1990), Geochronology of TAG and Snakepit hydrothermal fields, Mid-Atlantic Ridge: Witness to a long and complex hydrothermal activity, *Earth Planet. Sci. Lett.*, *97*, 113–128, doi:10.1016/0012-821X(90)90103-5.

Lalou, C., J.-L. Reyss, E. Brichet, P. Rona, and G. Thompson (1995), Hydrothermal activity on a 10^5-year scale at a slow-spreading ridge, TAG hydrothermal field, Mid-Atlantic Ridge 2°N, *J. Geophys. Res.*, *100*(B9), 17,855–17,862, doi:10.1029/95JB01858.

Langmuir, C., et al. (1997), Hydrothermal vents near a mantle hot spot: the Lucky Strike vent field at 37°N on the Mid-Atlantic Ridge, *Earth Planet. Sci. Lett.*, *148*, 69–91, doi:10.1016/S0012-821X(97)00027-7.

Le Douaran, S., and J. Francheteau (1981), Axial depth anomalies from 10 to 50° north along the Mid-Atlantic Ridge: Correlation with other mantle properties, *Earth Planet. Sci. Lett.*, *54*, 29–47, doi:10.1016/0012-821X(81)90066-2.

Lévêque, J.-L., L. Rivera, and G. Wittlinger (1993), On the use of the checker-board test to assess the resolution of tomographic inversions, *Geophys. J. Int.*, *115*, 313–318, doi:10.1111/j.1365-246X.1993.tb05605.x.

Lucazeau, F., A. Bonneville, J. Escartin, R. P. Von Herzen, P. Gouze, H. Carton, M. Cannat, V. Vidal, and C. Adam (2006), Heat flow variations on a slowly accreting ridge: Constraints on the hydrothermal and conductive cooling for the Lucky Strike segment (Mid-Atlantic Ridge, 37°N), *Geochem. Geophys. Geosyst.*, *7*, Q07011, doi:10.1029/2005GC001178.

Macdonald, K. (2001), Mid-ocean ridge tectonics, volcanism and geomorphology, in *Encyclopedia of Ocean Sciences*, pp. 1798–1813, Academic, London.

Magde, L., D. Sparks, and R. Detrick (1997), The relationship between buoyant mantle flow, melt migration and gravity bull's eyes at the Mid-Atlantic Ridge between 33°N and 35°N, *Earth Planet. Sci. Lett.*, *148*, 59–67, doi:10.1016/S0012-821X(97)00039-3.

Magde, L., A. Barclay, D. Toomey, R. Detrick, and J. Collins (2000), Crustal magma plumbing within a segment of the Mid-Atlantic Ridge, 35°N, *Earth Planet. Sci. Lett.*, *175*, 55–67, doi:10.1016/S0012-821X(99)00281-2.

Marques, A., F. Barriga, and S. Scott (2007), Sulfide mineralization in an ultramafic-rock hosted seafloor hydrothermal system: From serpentinization to the formation of Cu-Zn- (Co)-rich massive sulfides, *Mar. Geol.*, *245*, 20–39, doi:10.1016/j.margeo.2007.05.007.

Miller, D., and N. Christensen (1997), Seismic velocities of lower crustal and upper mantle rocks from the slow-spreading Mid-Atlantic Ridge, south of the Kane Transform Zone (MARK), *Proc. Ocean Drill. Program, Sci. Results*, *153*, 437–454.

Miranda, J., J. Luis, N. Lourenço, and F. Santos (2005), Identification of the magnetization low of the Lucky Strike hydrothermal vent using surface magnetic data, *J. Geophys. Res.*, *110*, B04103, doi:10.1029/2004JB003085.

Moreira, M., and C.-J. Allègre (2002), Rare gas systematics on Mid-Atlantic Ridge (37–40°N), *Earth Planet. Sci. Lett.*, *198*, 401–416, doi:10.1016/S0012-821X(02)00519-8.

Müller, R., W. Roest, J.-Y. Royer, L. Gahagan, and J. Sclater (1997), Digital isochrons of the world's ocean floor, *J. Geophys. Res.*, *102*(B2), 3211–3214, doi:10.1029/96JB01781.

Navin, D., C. Peirce, and M. Sinha (1998), The RAMESSES experiment: II. Evidence for accumulated melt beneath a slow spreading ridge from wide-angle refraction and multichannel reflection seismic profiles, *Geophys. J. Int.*, *135*, 746–772, doi:10.1046/j.1365-246X.1998.00709.x.

Ondréas, H., Y. Fouquet, M. Voisset, and J. Radford-Knoery (1997), Detailed study of three contiguous segments of the Mid-Atlantic Ridge, South of the Azores (37°N to 38°30′N), using acoustic imaging coupled with submersible observations, *Mar. Geophys. Res.*, *19*, 231–255, doi:10.1023/A:1004230708943.

Ondréas, H., M. Cannat, Y. Fouquet, A. Normand, P. M. Sarradin, and J. Sarrazin (2009), Recent volcanic events and the distribution of hydrothermal venting at the Lucky Strike hydrothermal field, Mid-Atlantic Ridge, *Geochem. Geophys. Geosyst.*, *10*, Q02006, doi:10.1029/2008GC002171.

Parson, L., E. Gràcia, D. Coller, C. German, and D. Needham (2000), Second-order segmentation: The relationship between volcanism and tec-

tonism at the MAR, 38°N–35°40′N, *Earth Planet. Sci. Lett.*, *178*, 231–251, doi:10.1016/S0012-821X(00)00090-X.

Perfit, M., and W. Chadwick Jr. (1998), Magmatism at mid-ocean ridges: Constraints from volcanological and geochemical observations, in *Faulting and Magmatism at Mid-Ocean Ridges*, *Geophys. Monogr. Ser.*, vol. 106, edited by W. R. Buck et al., pp. 59–115, AGU, Washington, D. C.

Purdy, G., and R. Detrick (1986), Crustal structure of the Mid-Atlantic Ridge at 23(N from seismic refraction studies, *J. Geophys. Res.*, *91*(B3), 3739–3762, doi:10.1029/JB091iB03p03739.

Schmeling, H. (1985), Numerical model on the influence of partial melt on elastic, anelastic and electric properties of rocks: Part I. Elasticity and anelasticity, *Phys. Earth Planet. Inter.*, *41*, 34–57, doi:10.1016/0031-9201(85)90100-1.

Schouten, H., K. D. Klitgord, and J. A. Whitehead (1985), Segmentation of mid-ocean ridges, *Nature*, *317*, 225–229, doi:10.1038/317225a0.

Shaw, P. (1994), Age variations of oceanic crust Poisson's ratio: Inversion and a porosity evolution model, *J. Geophys. Res.*, *99*(B2), 3057–3066, doi:10.1029/93JB02109.

Shaw, P., and J. Orcutt (1985), Waveform inversion of seismic refraction data and applications to young Pacific crust, *Geophys. J. R. Astron. Soc.*, *82*, 375–414.

Singh, S., W. Crawford, H. Carton, T. Seher, V. Combier, M. Cannat, J. Canales, D. Düsünür, J. Escartin, and J. Miranda (2006), Discovery of a magma chamber and faults beneath a Mid-Atlantic Ridge hydrothermal field, *Nature*, *442*, 1029–1032, doi:10.1038/nature05105.

Sinha, M., S. Constable, C. Peirce, A. White, G. Heinson, L. MacGregor, and D. Navin (1998), Magmatic processes at slow spreading ridges: Implications of the RAMESSES experiment at 57°45′N on the Mid-Atlantic Ridge, *Geophys. J. Int.*, *135*, 731–745, doi:10.1046/j.1365-246X.1998.00704.x.

Sinton, J., and R. Detrick (1992), Mid-ocean ridge magma chambers, *J. Geophys. Res.*, *97*(B1), 197–216, doi:10.1029/91JB02508.

Sleep, N. H. (1975), Formation of oceanic crust: Some thermal constraints, *J. Geophys. Res.*, *80*(29), 4037–4042, doi:10.1029/JB080i029p04037.

Spiess, F. N., et al. (1980), East Pacific Rise: Hot springs and geophysical experiments, *Science*, *207*(4438), 1421–1433, doi:10.1126/science.207.4438.1421.

Thibaud, R., P. Gente, and M. Maia (1998), A systematic analysis of the Mid-Atlantic Ridge morphology and gravity between 15°N and 40°N: Constraints of the thermal structure, *J. Geophys. Res.*, *103*(B10), 24,223–24,243, doi:10.1029/97JB02934.

Tolstoy, M., A. Harding, and J. Orcutt (1993), Crustal thickness on the Mid-Atlantic Ridge: Bull's-eye gravity anomalies and focused accretion, *Science*, *262*(5134), 726–729, doi:10.1126/science.262.5134.726.

Toomey, D., D. Jousselin, R. Dunn, W. S. D. Wilcock, and R. Detrick (2007), Skew of mantle upwelling beneath the East Pacific Rise governs segmentation, *Nature*, *446*, 409–414, doi:10.1038/nature05679.

Weiss, R., P. Lonsdale, J. Lupton, A. Bainbridge, and H. Craig (1977), Hydrothermal plumes in the Galapagos rift, *Nature*, *267*, 600–603, doi:10.1038/267600a0.

Wepfer, W., and N. Christensen (1991a), A seismic velocity-confining pressure relation, with applications, *Int. J. Mech. Min. Sci. Geomech. Abstr.*, *28*(5), 451–456, doi:10.1016/0148-9062(91)90083-X.

Wepfer, W., and N. Christensen (1991b), Q structure of the oceanic crust, *Mar. Geophys. Res.*, *13*, 227–237, doi:10.1007/BF00369151.

Wilcock, W. S. D., M. Dougherty, S. Solomon, G. Purdy, and D. Toomey (1993), Seismic propagation across the East Pacific Rise: Finite difference experiments and implications for seismic tomography, *J. Geophys. Res.*, *98*(B11), 19,913–19,932, doi:10.1029/93JB01820.

Wilkens, R., G. Fryer, and J. Karsten (1991), Evolution of porosity and seismic structure of upper oceanic crust: Importance of aspect ratios, *J. Geophys. Res.*, *96*(B11), 17,981–17,995, doi:10.1029/91JB01454.

Wright, T., C. Ebinger, J. Biggs, A. Ayele, G. Yirgu, D. Keir, and A. Stork (2006), Magma-maintained rift segmentation at continental rupture in the 2005 Afar dyking episode, *Nature*, *442*, 291–294, doi:10.1038/nature04978.

Yang, T., Y. Shen, S. van der Lee, S. Solomon, and S.-H. Hung (2006), Upper mantle structure beneath the Azores hotspot from finite-frequency seismic tomography, *Earth Planet. Sci. Lett.*, *250*, 11–26, doi:10.1016/j.epsl.2006.07.031.

Zelt, C. (1998), Lateral velocity resolution from three-dimensional seismic refraction data, *Geophys. J. Int.*, *135*, 1101–1112, doi:10.1046/j.1365-246X.1998.00695.x.

Zelt, C. (1999), Modelling strategies and model assessment for wide-angle seismic traveltime data, *Geophys. J. Int.*, *139*, 183–204, doi:10.1046/j.1365-246X.1999.00934.x.

Zelt, C. A., and D. A. Forsyth (1994), Modeling wide-angle seismic data for crustal structure: Southeastern Greenville Province, *J. Geophys. Res.*, *99*(B6), 11,687–11,704, doi:10.1029/93JB02764.

M. Cannat, V. Combier, W. C. Crawford, D. Dusunur, and S. C. Singh, Institut de Physique du Globe de Paris, Géosciences Marines, Boite 89, 4 Place Jussieu, F-75252 Paris CEDEX 05, France.

T. Seher, Earth Resources Laboratory, Massachusetts Institute of Technology, 77 Massachusetts Ave., 54-511, Cambridge, MA 02139-4307, USA.